Final Report to

Petrophysical Studies of Unconventional Gas Reservoirs Using High-resolution Rock Imaging

Project Number 07122-22.FINAL

November 30 2012

Dmitriy Silin (PI)
DSilin@lbl.gov

Timothy J. Kneafsey
TJKneafsey@lbl.gov

Earth Sciences Division
Lawrence Berkeley National Laboratory
1 Cyclotron Road
MS 90R1116
Berkeley, CA 94720
1-510-486-6455
http://esd.lbl.gov/home/

LEGAL NOTICE

This report was prepared by Lawrence Berkeley National Laboratory as an account of work sponsored by the Research Partnership to Secure Energy for America, RPSEA. Neither RPSEA, members of RPSEA, the National Energy Technology Laboratory, the U.S. Department of Energy, nor any person acting on behalf of any of the entities:

a. MAKES ANY WARRANTY OR REPRESENTATION, EXPRESS OR IMPLIED WITH RESPECT TO ACCURACY, COMPLETENESS, OR USEFULNESS OF THE INFORMATION CONTAINED IN THIS DOCUMENT, OR THAT THE USE OF ANY INFORMATION, APPARATUS, METHOD, OR PROCESS DISCLOSED IN THIS DOCUMENT MAY NOT INFRINGE PRIVATELY OWNED RIGHTS, OR

b. ASSUMES ANY LIABILITY WITH RESPECT TO THE USE OF, OR FOR ANY AND ALL DAMAGES RESULTING FROM THE USE OF, ANY INFORMATION, APPARATUS, METHOD, OR PROCESS DISCLOSED IN THIS DOCUMENT.

THIS IS A FINAL REPORT. THE DATA, CALCULATIONS, INFORMATION, CONCLUSIONS, AND/OR RECOMMENDATIONS REPORTED HEREIN ARE THE PROPERTY OF THE U.S. DEPARTMENT OF ENERGY.

REFERENCE TO TRADE NAMES OR SPECIFIC COMMERCIAL PRODUCTS, COMMODITIES, OR SERVICES IN THIS REPORT DOES NOT REPRESENT OR CONSTITUTE AN ENDORSEMENT, RECOMMENDATION, OR FAVORING BY RPSEA OR ITS CONTRACTORS OF THE SPECIFIC COMMERCIAL PRODUCT, COMMODITY, OR SERVICE.

This page is intentionally left blank.

SIGNATURE AND DATE STAMP

Timothy J. Kneafsey P.E., Ph.D.

Principal Investigator's signature:

Date: November 30 2012

ABSTRACT

The main objective of this work is to determine (a) the physical mechanisms that limit gas recovery from tight rock formations, and (b) the means of extending this recovery as far into the future as possible. Because the mechanisms that block gas flow in the formation and near the wellbore are not fully understood, we propose to use the sophisticated petrophysical imaging tools and theoretical calculation methods at our disposal to elucidate these mechanisms. Once we better understand the key factors that influence the rate and ultimate level of gas recovery, we will investigate methods of changing the formation properties volumetrically to optimize production in space and in time.

Table of Contents

SIGNATURE AND DATE STAMP 3

ABSTRACT 4

FIGURES AND/OR TABLES 6

EXECUTIVE SUMMARY 10

INTRODUCTION 11

TASK 4: 3D IMAGING OF THE PORE SPACE OF SHALE USING THE FOCUSED ION BEAM/SCANNING ELECTRON MICROSCOPY 12

OBJECTIVES 12
METHODS 12
RESULTS AND DISCUSSIONS 14
DIAMOND KNIFE / SEM TECHNIQUE VERSUS FIB/SEM IMAGING 19
APPLICATION TO PRODUCTION DECLINE ANALYSIS 20

TASK 5: 3D IMAGING OF THE PORE SPACE OF TIGHT SANDS 23

OBJECTIVES 23
METHODS 23
OPTICAL MICROSCOPY 24
LOW-RESOLUTION TOMOGRAPHY 25
X-RAY MICROTOMOGRAPHY AT THE ALS 30
SEM IMAGING OF MICROPOROSITY 31
SUBMICRON-RESOLUTION TOMOGRAPHY 32
RESULTS AND DISCUSSIONS 34
RESOLUTION GAP 37

TASK 6: A MODEL OF RETROGRADE CONDENSATION AT THE MATRIX-FRACTURE INTERFACE 38

OBJECTIVES 38
METHODS 39
RESULTS AND DISCUSSIONS 39

TASK 7: PREDICTION OF PETROPHYSICAL ROCK PROPERTIES FORM PORE SPACE GEOMETRY 42

SUBTASK 7.1. MODELING KLINKENBERG EFFECT: FLOW WITH SLIPPAGE 42
OBJECTIVES 42

METHODS 42
RESULTS AND DISCUSSIONS 43
BOUNDARY CONDITION 44
SUBTASK 7.2. TWO-PHASE FLOW PROPERTIES: THE MIS METHOD 46
OBJECTIVES 46
METHODS 47
THE METHOD OF MAXIMAL INSCRIBED SPHERES 47
EVALUATION OF PERMEABILITY AND RELATIVE PERMEABILITY CURVES 48
RESULTS AND DISCUSSIONS 50

TASK 8: COMPUTER MODELS OF TIGHT GAS ROCKS 55

OBJECTIVES 55
METHODS 56
RESULTS AND DISCUSSIONS 56

CONCLUSIONS 60

ACKNOWLEDGEMENTS 62

LITERATURE 63

IMPACT TO PRODUCERS 68

TECHNOLOGY TRANSFER EFFORTS 68

LIST OF ACRONYMS AND ABBREVIATIONS 71

APPENDICES 71

FIGURES and/or TABLES

Figure 1. Sequence of images collected at 25 nm spacing. 13

Figure 2. Left: Schematic of FIB/SEM configuration; Right: Interior of the FIB/SEM (see [58]). .. 13

Figure 3. 3D reconstrauction (A) and a single slice (B) diamond knife / SEM images of Marcellus shale. The images are courtesy of Gatan, Inc. 14

Figure 4. X-ray computed tomography cross sections of a shale sample showing anisotropy and heterogeneity. The scale bar is approximate density in g/cm^3 and the sample is about 2.5 cm in diameter. a. x-y cross section, b. y-z cross section. 15

Figure 5. Coarse and fine images of FIB milled and polished shale surfaces. Coarse images indicate that the REV is larger than the imaged area, however, the fine images indicate that more information is needed at the nanometer scale. 16

Figure 6. Images of FIB milled and polished shale surfaces. The three shales in the right column are from different locations in the same formation. 17

Figure 7. New Albany shale sample shows high organic contents, but almost zero porosity in kerogen. The arrow points to a fossil algae inclusion. 18

Figure 8. a. – Framboidal pyrite inclusion in New Albany shale sample; b. – 3D reconstruction of the pyrite grain pack; c. – pore space and streamline of flow simulation in the x direction. 19

Figure 9. The flow geometry schematic in multistage-fractured gas well. 21

Figure 10. Data and type curve in semi-log coordinates. 22

Figure 11. The diamonds show model-predicted total gas recovery over 87 months based on the number of months of production on the horizontal axis. The actual total recovery over the same 87 months is shown as a horizontal solid line. The dashed lines show ±5 % relative error range centered at the actual recovery. 22

Figure 12. Micrographs of tight sand a. Sample 1, b. Sample 2, c. Sample 4, and d. Sample 5. ... 25

Figure 13. The original image (left), shows pixels brightening near sample boundaries, which is a beam-hardening artifact. The picture on the right shows this artifact removed. 26

Figure 14. The intensity along the line AB, Fig. 13, before (blue dashed line) an after (red solid line) beam hardening removal shows that beam hardening can hide important features. . 27

Figure 15. X-ray CT images of Sample 1 (a) axial cross section, (b) cross section along vertical central plane of (a), and (c) cross section along horizontal central cross section of (a), (d) photograph of core. The sample is 36 mm in diameter. 28

Figure 16. X-ray CT images of Sample 2: (a) axial cross section, (b) cross section along vertical central plane of (a), and (c) cross section along horizontal central cross section of (a), (d) photograph of core. The sample is 23 mm in diameter. 29

Figure 17. X-ray CT images of Sample 3: (a) axial cross section, (b) cross section along vertical central plane of (a), and (c) cross section along horizontal central cross section of (a), (d) photograph of core. The sample is 22 mm in diameter. 30

Figure 18. SEM 4000x magnification images show different types of clay plates contribute to the microporosity of the sample: kaolinite (a) and montmorillonite (b). 32

Figure 19. A micro CT reconstruction, on the left, accurately reproduces a planar cross-section of a sample, whereas a SEM image, on the right displays the rough surface of the sample. ... 32

Figure 20. A slice of microtomgraphy data at 500 nm resolution shows high contrast and very low level of noise. The image is courtesy of Xradia, Inc. 33

Figure 21. A 0.5x 0.5x 0.5 mm tight-sand sample at 500 nm resolution. Micro CT data are courtesy of Xradia, Inc. 34

Figure 22. Two-dimensional cross-sections of micro-CT images of conventional outcrop sandstone (a) and tight sand (b) samples at resolutions of 4.5 and 1.8 microns, respectively. 35

Figure 23. Two-dimensional cross-sections of micro-CT images of tight sand samples. Voxel size is 1.8 microns, except the top right image, where the voxel size is 0.9 micron. The samples are numbered 2–5 row-wise, starting from the top left image. 36

Figure 24. A 3D reconstruction of a tight sand sample of dimensions 0.7 mm^3. Narrow, just a few microns, slit-like pores result in a very low permeability and make simulations very challenging task. 37

Figure 25. Clay filling of pores and submicron aperture slit-like pores in tight gas sand. The images are courtesy of Xradia, Inc. 38

Figure 26. Phase diagram of hydrocarbon mixture(modified from[39]). The shaded zone denotes gas-condensate system, the dashed line corresponds to the reservoir temperature, and the diamond denotes the initial reservoir conditions. 39

Figure 27. A schematic of liquid-saturated skin at matrix-fracture interface 41

Figure 28. Evaluation of dimensionless estimated ultimate recovery as a function of u_f shows strong impact of fracture pressure. The optimal recovery estimate exceeds the best constant-pressure result by approximately 20 %. 42

Figure 29. Estimated permeability versus slippage coefficient. The permeability is normalized with no-slip flow. 46

Figure 30. A schematic 2D illustration of the method of maximal inscribed spheres: The area swept by inscribed spheres of a given radius determines the part of the pore space occupied by the nonwetting fluid. The radius decreases at increasing capillary pressure. The picture in Exhibit A corresponds to a capillary pressure lower than that in exhibit B. 47

Figure 31. Gray-scale micro CT image (A) and MIS calculated two-phase fluid distribution in a 2 x 2 x 2 mm^3 sample of sandstone. The 4.5 μm resolution CT data were acquired by Jonathan Ajo-Franklin at the Advanced Light Source facility of LBNL. 48

Figure 32. Examples of dead-end voxel configurations. 49

Figure 33. The impact of cluster-search cleanup on the capillary pressure curve evaluation. 51

Figure 34. Computed gas distribution in the pores before (left) and after (right) being disconnected. 52

Figure 35. Capillary pressure curves evaluated from invasion percolation in three coordinate directions: x (left), y (middle), and z (right). 52

Figure 36. Computed relative permeability curves and laboratory data (circles). The laboratory data are courtesy of Statoil. 53

Figure 37. Computed relative permeability data (diamonds for imbibition and crosses for drainage) and laboratory measurements (triangles for imbibition and squares for drainage) of gas relative permeability for different water saturations. The solid lines display mean computed imbibition relative permeability curves, and the dashed curves show mean computed drainage relative permeability curves. The laboratory data are courtesy of Chevron. 54

Figure 38. Evaluation of relative permeability curves using MIS analysis and flow simulations. Diamonds denote imbibition relative permeabilities, crosses correspond to drainage. The solid lines show mean imbibition, and the dashed lines show mean drainage curves. 54

Figure 39. Digitized computer-generated porous structure, on the left, and gray-scale micro CT data for a sample of Bentheim sandstone with voxel size 4.42 μm, on the right. 56

Figure 40. Dimensionless capillary pressure evaluated from images of computer-generated and natural rock samples for two different contact angles (CA). 57

Figure 41. Computer-generated structure with slit-like narrow pores 57

Figure 42. Dimensionless capillary pressure curves computed for different resolutions and two contact angles 58

Figure 43. Relative permeability curves evaluated for media with slit-like pores evaluated for zero, (a), and 60^{o}, (b), contact angles. 59

Figure 44. Computer-generated structures to mimic pore fillings by clay, *cf* Figure 18. 59

EXECUTIVE SUMMARY

The main objective of this work was to determine (a) the physical mechanisms that limit gas recovery from tight rock formations, and (b) the means of extending this recovery as far into the future as possible. Because the mechanisms that block gas flow in the formation and near the wellbore are not fully understood, we used sophisticated petrophysical imaging tools and theoretical calculation methods at our disposal to elucidate these mechanisms. We gained a better understanding of the key factors that influence the rate and ultimate quantity of gas recovery, and investigated methods of changing the formation properties volumetrically to optimize production in space and in time

We acquired high-resolution images of gas-bearing shale rocks using the Advanced Light Source (ALS) facility and Focused Ion Beam (FIB) technology at the Molecular Foundry and the National Center for Electron Microscopy at Lawrence Berkeley National Laboratory (LBNL), and analyzed these images using Maximal Inscribed Spheres-type methods in order to estimate gas shale and tight sand flow properties at different, including *in situ*, conditions. These approaches have been developed at LBNL and University of California at Berkeley (UCB) and have been successfully applied to studies of chalk, diatomite, and sandstone. We investigated the impact of pore-space geometry in different rock formations on flow properties, including absolute and relative permeabilities, capillary pressure, and Klinkenberg coefficient. The 3D images of the rocks acquired in this project may help to develop depositional models and to link the petrophysical properties of the rock to the geology and geological history of the reservoir.

A thorough and comprehensive study of existing unconventional gas-bearing formations will create a knowledge base for the development of emerging and frontier developments. Our study is fundamental, and acquired knowledge will be equally applicable in short- and long-term technology developments.

This work has been performed at Lawrence Berkeley National Laboratory (LBNL) of the U.S. Department of Energy (DOE) under Contract No. DE-AC02-05CH11231. Portions of this work were performed at the Advanced Light Source facility, Molecular Foundry and The National Center for Electron Microscopy (NCEM), LBNL, which are supported by the Office of Science, Office of Basic Energy Sciences, of the U.S. Department of Energy under Contract No. DE-AC02-05CH11231.

Introduction

Understanding the processes that affect natural gas movement in tight shale formations, and the behavior of fluids (flow, condensation, effects of other fluids) in these formations is important to allow expansion and optimization of gas recovery techniques. The physical mechanisms that limit gas recovery from tight rock formations depend on the location of the gas and the geometry of the porespace. Extending gas recovery as far into the future as possible requires an appropriate understanding of flow processes through shale, fractures, the near-well environment, and the well. Because the mechanisms that block gas flow in the formation and near the wellbore are not fully understood, sophisticated petrophysical imaging tools and theoretical calculation methods are used to elucidate these mechanisms. Once the key factors that influence the rate and ultimate quantity of gas recovery are understood, methods of changing the formation properties volumetrically to optimize production in space and in time can be developed. The usual approach of highly discounting the future recovery may no longer be applicable in a world in which real energy prices will be growing faster than the local (*e.g.*, state) economies.

In this work, we present high-resolution images of gas-bearing shale rocks using the Advanced Light Source (ALS) micro-computed tomography facility and Focused Ion Beam (FIB) technology at the Molecular Foundry and the National Center for Electron Microscopy at Lawrence Berkeley National Laboratory (LBNL). We analyze these images using Maximal Inscribed Spheres-type methods in order to estimate gas shale and tight sand flow properties at different conditions, including *in situ* conditions. These approaches have been developed at LBNL and University of California at Berkeley (UCB) and have been successfully applied to studies of chalk, diatomite, and sandstone. We have investigated the impact of pore-space geometry in different rock formations on flow properties, including absolute and relative permeabilities, capillary pressure, and the Klinkenberg coefficient.

Our report describes our examination of appropriate tight rock samples including shales and tight sandstones at various scales from photographic, microscopic, X-ray computed tomography (CT), micro-computed tomography, and Focused Ion Beam/Scanning Electron Microscopy (FIB/SEM). We present models of gas production, the effects of retrograde condensation, prediction of two-phase flow properties from petrophysical image collections, and computer models of tight gas rocks.

Task 4: 3D imaging of the pore space of shale using the Focused Ion Beam/Scanning Electron Microscopy

Objectives

The main objective of this task is to study of the pore structure of gas shale samples. Visualization of nanometer-scale pores in gas shale, chalk requires powerful tools. Most of these tools were developed only in the past decades. To resolve the 3D pore structure, LBNL team used focused ion beam (FIB) technology [57,58]. It includes milling layers as thin as 10 nanometers from the sample using accelerated Ga^+ ions. After each milling step, a 2D image of this fresh surface is generated by Scanning Electron Microscopy (SEM) or ion beam imaging. The 2D images are then stacked to reconstruct the 3D pore or grain structure. Appropriate currents were determined to optimize the balance between resolution and imaging time for the samples of interest in each individual case. Micro-scale diffraction analysis was used to resolve the mineral composition of the sample.

Methods

To understand gas and liquid flow through shales, an understanding of their pore structure is required. For common earth media, the pore space is easily conceived as the space between the assorted grains that make up the medium. While still conceptually true for shales, imaging of the structure at the pore scale is necessary to understand this space. To obtain the three-dimensional structure of shale samples and their pore space, we imaged samples using a scanning electron microscope (SEM) coupled with a focused ion beam (FIB) to provide milling capability. The FIB/SEM instrument, housed at the Molecular Foundry at Lawrence Berkeley National Laboratory, is a Zeiss XB1540 EsB having a GEMINI® field emission column (FESEM) with the Orsay Physic focused ion beam. The instrument has a maximum resolution of 1.1 nm at 20 kV and 2.5 nm at 1 kV, the FIB column uses a liquid gallium source and has a resolution of 7-5 nm at 30 kV. Sample manipulation is performed on a 6-axis fully eucentric motorized stage.

Samples were prepared by machining a flat surface using standard machining tools on a shale coupon having dimensions of about 6 mm × 6 mm × 1 mm. Although the standard machining tools leave scratch marks in the coupon that are visible under optical and electron microscopy, the scale of the scratches is on the order of the scale of the region imaged, thus there is ample sample area for imaging that is reasonably undisturbed. The samples were attached to the stub using conductive tape, and coated with about 4.5 nm of platinum prior to milling and imaging.

To obtain a three-dimensional description of the porespace, the FIB mills a flat surface which is then imaged using the SEM. The process is repeated a number of times, each time milling a fixed thickness of sample (Figure 1). Thicknesses of the milled slices depend on the milling current, with high currents (order of nA) milling thicker and less precise slices. Slices presented in this paper have thicknesses ranging from 25 nm to 75 nm. Registering (aligning) and stacking the images provides a three dimensional digital reconstruction of the sample, which can then be manipulated by computer. In the FIB/SEM system, the electron beam and ion beam are

positioned 54 degrees from each other (Figure 2). Because of this configuration, any reasonably flat location on a sample can be milled and imaged. To avoid repositioning the sample so that the surface is orthogonal to the SEM following each FIB slice, the SEM images are adjusted to account for the angle.

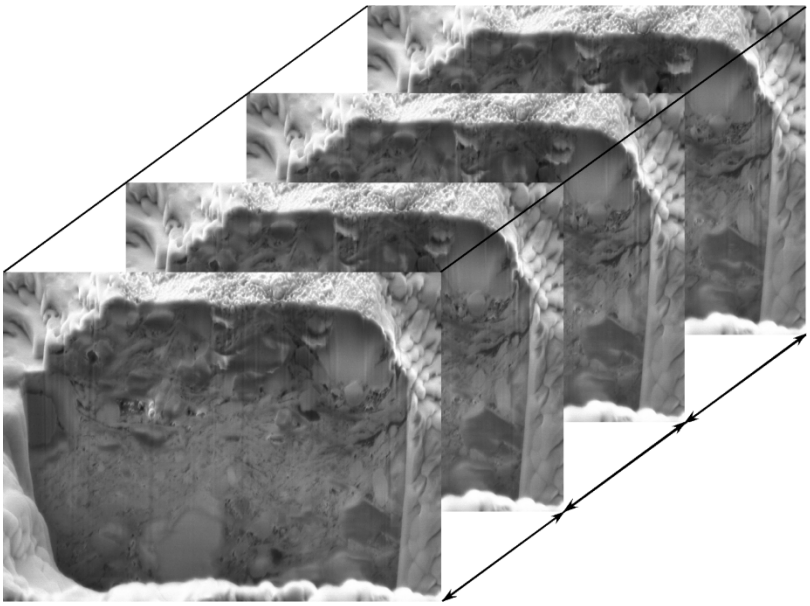

Figure 1. Sequence of images collected at 25 nm spacing.

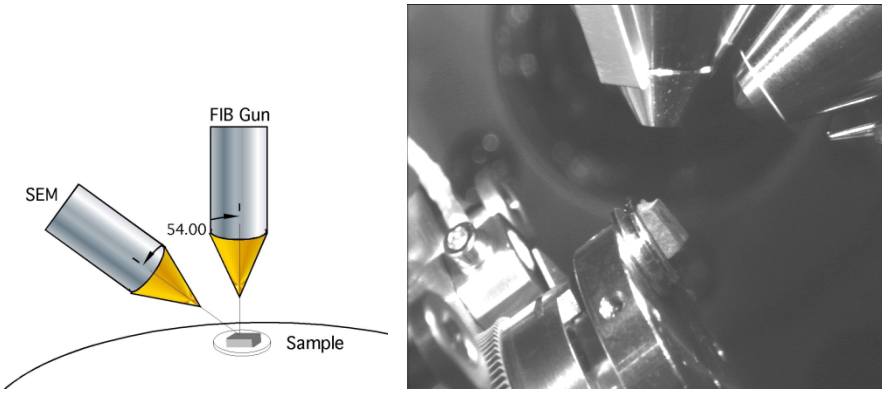

Figure 2. Left: Schematic of FIB/SEM configuration; Right: Interior of the FIB/SEM (see [58]).

One of the limitations of FIB/SEM approach is the small size of the study area. Although broad ion-beam (BIB) milling can polish a large area for SEM imaging, we are unaware of a sequential BIB/SEM milling and imaging technique for acquiring 3D data. Another method that can be used to view sequential slices of a sample is diamond knife cutting with SEM imaging (Joel Mancuso. Gatan, Inc.). Figure 3 exhibit A shows a 3D reconstruction with voxel size of 50 nm, whereas Figure 3 exhibit B shows a single slice of this reconstruction using the diamond knife technique. An artifact of this technique is “pull-out” of grains which may result in overestimation of porosity, false pores, and residual pulled-out grains obstructing the fresh surface.

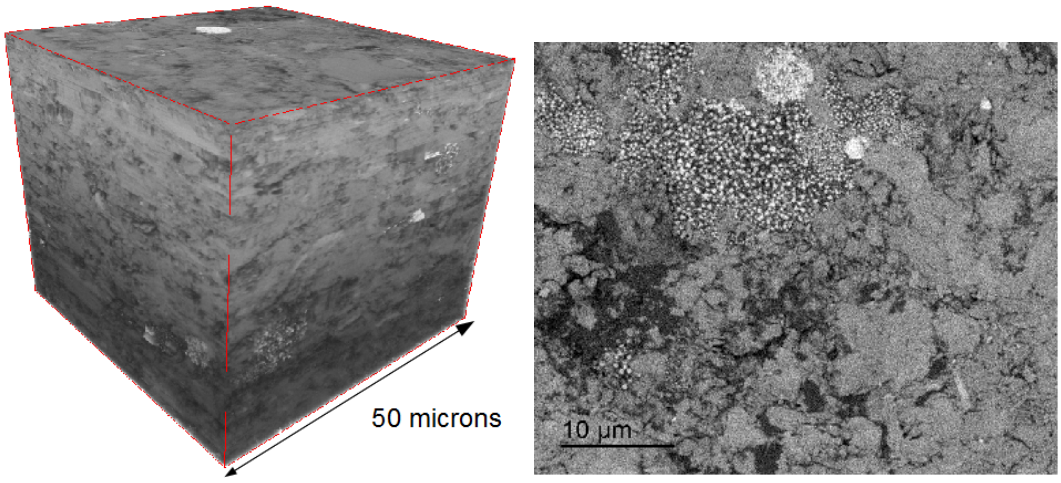

Figure 3. 3D reconstrauction (A) and a single slice (B) diamond knife / SEM images of Marcellus shale. The images are courtesy of Gatan, Inc.

Results and Discussions

First, when performing nanometer-scale examinations of shale samples, it is important to consider the scale of the observation and the scale of interest. We typically image a volume of about 20 μ m $\times$ 10 μ m $\times$ 5 μ m, whereas a shale zone may be on the order of 100 km $\times$ 100 km $\times$ 0.1 km. In comparing the scales, it is clear that our sample is approximately 27 orders of magnitude (roughly 1000 times Avogadro's number) smaller than the shale zone. Even if compared to the shale volume contributing to a single well, the sample is still 20 orders of magnitude smaller. Thus, the relative scale must be considered.

Second, the sampling bias must be considered. Shales are anisotropic and contain heterogeneities across a variety of scales. Figure 4 presents three orthogonal cross sections from x-ray computed tomography scanning showing the density map across those cross sections. The sample has distinct heterogeneities, anisotropy from the bedding is clear, and if the mineralogy is consistent, the porosity must vary between layers. It is probable that the permeability varies between layers as well. Fractures are one of the most important features of a gas-producing shale [24]. Because these are relatively highly porous and often mechanically weak and thus difficult to machine for examination, they are not often examined in spite of their importance.

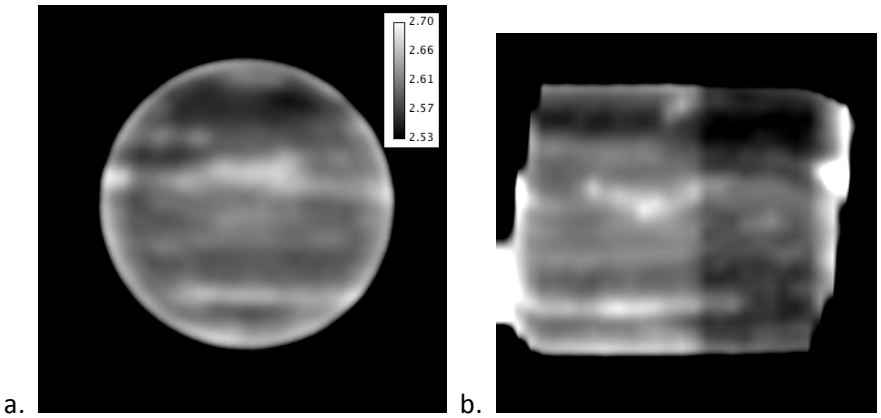

Figure 4. X-ray computed tomography cross sections of a shale sample showing anisotropy and heterogeneity. The scale bar is approximate density in g/cm^3 and the sample is about 2.5 cm in diameter. a. x-y cross section, b. y-z cross section.

Third, the effects of sampling, sample handling, dessication, and machining all place stress on the sample and must be considered. Even the FIB affects the sample, particularly at high current, thus lower currents are used for polishing and prior to collecting images. Small cracks in the sample may be a result of machining, so clues to their nature such as the presence of clay particles within the fracture need to be sought.

Fourth, to truly use the 3-D pore structure for flow simulations and to scale up, the size of the representative elementary volume needs to be determined. This can be done independently of the fracture network, which imposes another scale of interest, as an understanding of gas transport within the shale itself is required.

While recognizing these concerns about nanometer-scale imaging of shales, we also recognize that there are a number of important reasons to perform this imaging. From the images one can often get an understanding of the three-dimensional nature of the pore space, its connectivity, and the location and distribution of mineral and organic phases. In addition, the images provide a baseline for conceptual model building. In this report, we will present images from nine different shales and compare observed features.

Figures 5 and 6 present images from eight different shales from different regions of the US. Figure 5 shows both coarse (~ 25 micron field of view) and fine (~10 micron field of view) images to better show small-scale features. Figure 6 shows three different shales in the left column, and three images of Marcellus shale from different locations in the right column. In spite of the various locations, there are many similarities between samples. First, all contain small pores, seen as dark spots or curves on the images. All are composed of both rounded mineral grains and sheet-like clays. The samples have varying porosity, however, and varying degrees of porosity interconnectedness.

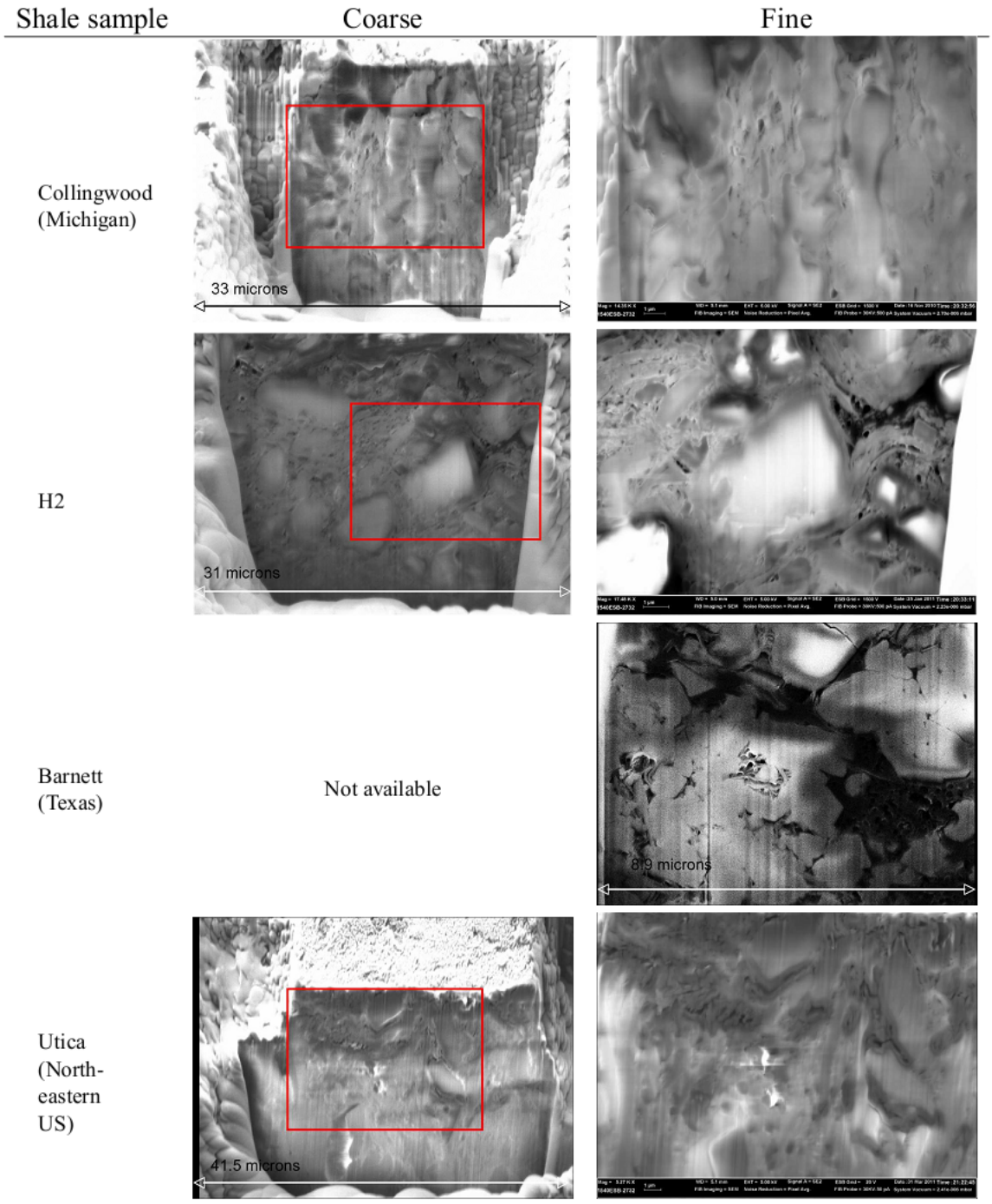

Figure 5. Coarse and fine images of FIB milled and polished shale surfaces. Coarse images indicate that the REV is larger than the imaged area, however, the fine images indicate that more information is needed at the nanometer scale.

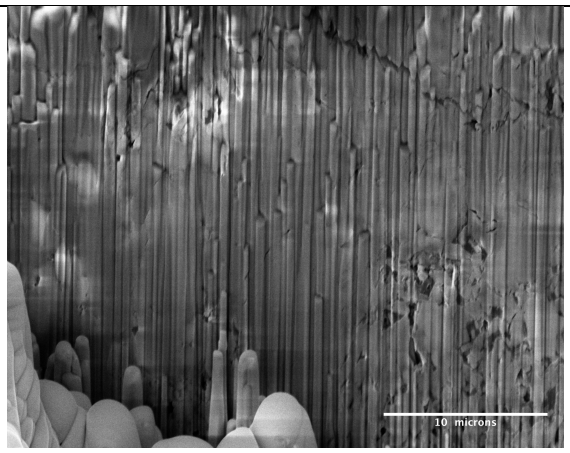

Eagleford

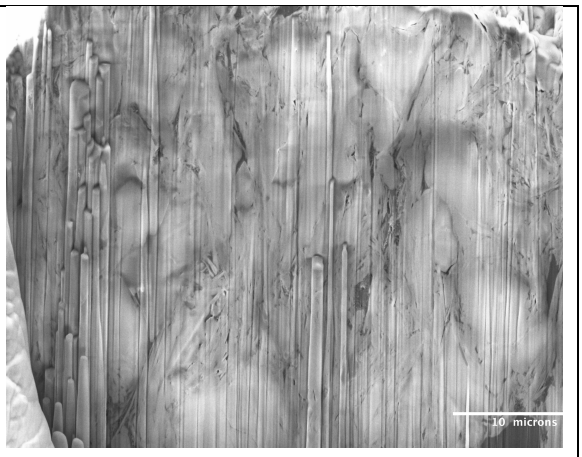

Marcellus

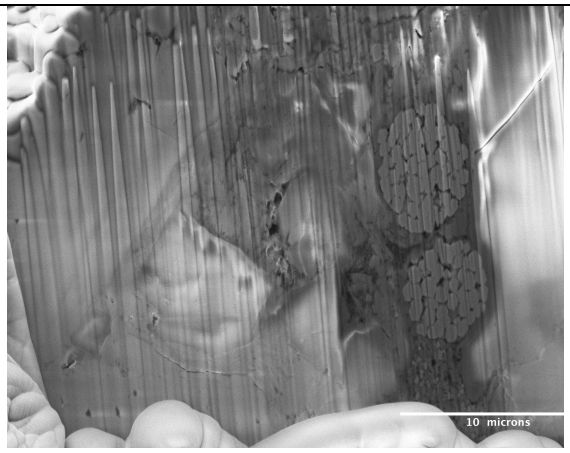

Montney

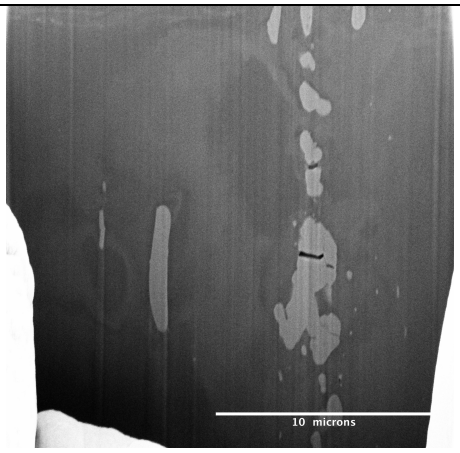

Marcellus

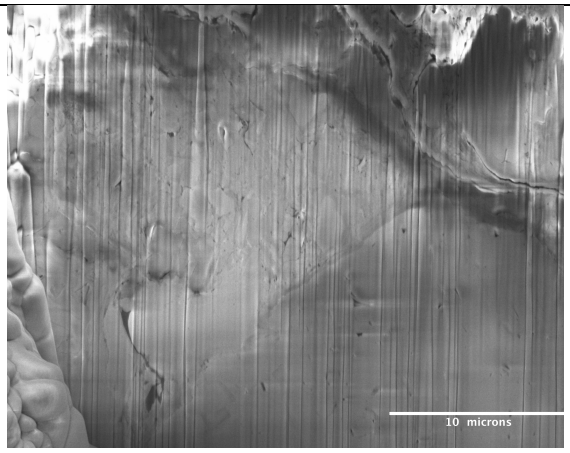

Kern

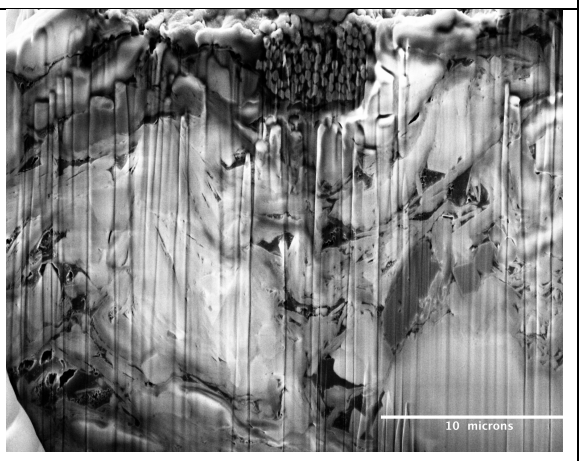

Marcellus

Figure 6. Images of FIB milled and polished shale surfaces. The three shales in the right column are from different locations in the same formation.

In the Collingwood shale, many of the pores have aspect ratios that are on the order of $1:1:1$ ($x:y:z$). Some penny-shaped pores are present as well, but there is little visible interconnected porosity on this scale for gas flow. In contrast to that, the H2 shale sample shows a suspension of large mineral grains (*e.g.* white grain in the center of the right image) within a porous matrix composed mostly of sheet-like clays. The pores tend to resemble these sheet-like clays in shape, and are somewhat tortuously interconnected. Some of these elongated pores are on the order of 100 nm in aperture, although this dimension is quite spatially variable. The Barnett sample we imaged contained both sheet-like clays, and a relatively larger fraction of rounded mineral grains. In addition, we can see an organic-rich phase (dark, lower left) that contains numerous spherical voids. This organic-rich phase is directly connected to the tortuous connected pore space, composed of the space between somewhat randomly distributed compacted sheet-like and rounded particles. There is a clear connected pore space in this sample that would allow gas flow away from the likely source. The Utica sample we imaged contained a region of tortuously connected pore space adjacent to a tight, nonporous region. The material surrounding the connected pore space appears darker in the images, indicating that its material properties are somewhat different from the material less than a micron away.

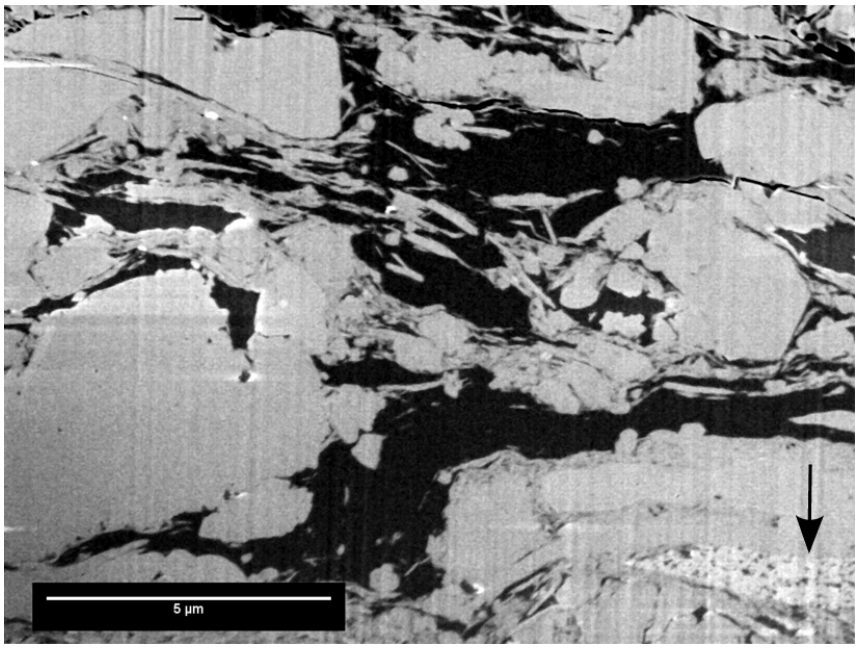

Figure 7. New Albany shale sample shows high organic contents, but almost zero porosity in kerogen. The arrow points to a fossil algae inclusion.

The New Albany shale sample, Figure 7, has a high organic carbon content not seen in most of the imaged samples, however the connected pore space is relatively difficult to discern. This property of the images of New Albany shale is in contrast with 30-40% porosity observed in kerogen in the Barnett shale sample (Figure 5). Note the fossil micro-algae in the right-bottom corner of the image in Figure 7.

a.

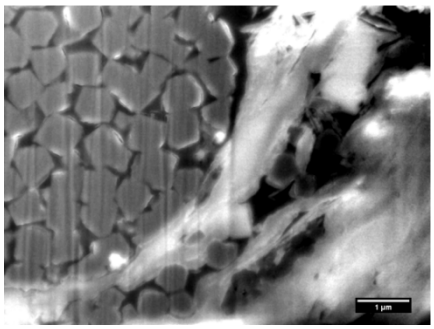

b.

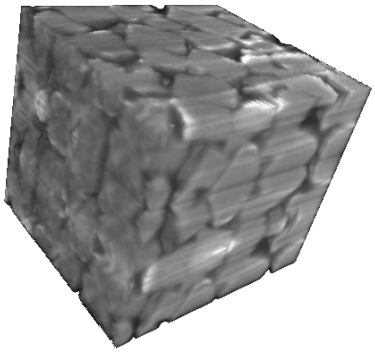

c.

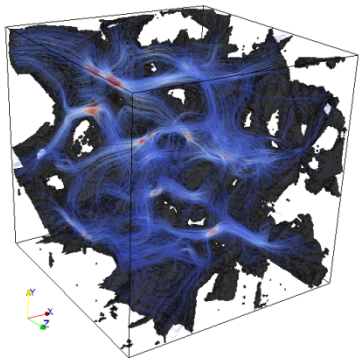

Figure 8. a. – Framboidal pyrite inclusion in New Albany shale sample; b. – 3D reconstruction of the pyrite grain pack; c. – pore space and streamline of flow simulation in the x direction.

From imaging many samples, we are beginning to gain an understanding of the nature of the pore space in a variety of shales. Our understanding of fluid flow through these pores is informed by segmenting and extracting the pore space from the three dimensional image stacks, and computationally analyzing fluid flow through these pores aided by modeling tools. In some cases, three-dimensional image analysis can offer opportunities that are hardly available in the laboratory. For example, Figure 8 shows an image of New Albany shale sample with a framboidal pyrite structure. Dispersed pyrite inclusions were practically the only parts of the scanned New Albany samples showing noticeable porosity. The image in Figure 8 a. displays the grains in high contrast, because of the high density of pyrite. Flow simulations produce permeability estimates in the order of microdarcy, even though the porosity was estimated between 30 and 40%. Note that a laboratory study of the flow properties of individual components of reservoir shale would hardly be possible.

Diamond knife / SEM technique versus FIB/SEM imaging

Thus far, we are unaware of any published works about diamond-knife / SEM imaging applications to imaging shale. Thus, the study conducted within this project is new and unique. A comparison between this method and FIB/SEM cannot determine which out of these two techniques is the best one. Diamond-knife / SEM beats FIB/SEM with regard to simplicity and automation. The volume shown in Figure 3 A is more than ten times larger than in FIB/SEM images, and all image slices were acquired in fully automated mode. The way the process is

setup eliminates the necessity of refocusing SEM as layers of material are removed by the diamond knife. The reason is that the plane of the surface exposed for imaging always remains at the same place. The system only must assure that the sample advancements between sequential image acquisitions must be the same. In early FIB/SEM studies [57,58], refocusing was done manually and it was an extremely time-consuming operation until the manufacturers automated this function in the newer machines. Once set up, the FIB technique can automatically collect hundreds of sequential images, but at some point, the milled material may obscure the field of vision.

At the same time, diamond knife cutting is more intrusive than FIB milling. As our studies revealed, shale texture is very heterogeneous, even of the area of study is just tens of microns. Grains and inclusions of different minerals with different mechanical properties react on the cutting differently. Instead of cutting some grains, the knife yanks them from their locations and drags them over the imaged surface. Consequently, the imaged structure can differ from the pore geometry in pristine state.

There are issues pertinent to both approaches. For example, in both cases the quality of data may be affected by charging. Unlike computed tomography data, the images show not just the slices of the material, but also some parts behind the image plane. The latter circumstance drastically complicates image segmentation and quantitative study of the pore space geometry.

Application to production decline analysis

In spite of the rich variety of the gas-shale structures revealed by the imaging study, all studied samples show very low permeability of the rock matrix. This observation lead us to a model of gas flow to a fractured well. In this model, the permeability of the pristine reservoir is negligible, and gas flow occurs only in the limited stimulated reservoir volume adjacent to the fracture. Exhibit A in Figure 9 shows a schematic of the conceptual model for a multi-stage fractured horizontal well employed in this study. In this model, pristine reservoir rock is practically impermeable. Gas flows only in the stimulated reservoir volume adjacent to the main hydraulic fractures. The horizontal portion of the well crosses a series of such fractures. The stimulated volumes connected to neighboring principal fractures are separated by no-flow boundaries. This no-flow boundary is determined either by the depth of stimulated volume, or the separation between two fracture feeding zones. We hypothesize that the geometric form of the stimulated zone feeding a fracture represents a slab parallel to the fracture face. Exhibit B in Figure 9 shows the geometry of a plan view (view from above) of the stimulated volume crossed by the horizontal portion of well. We assume that the permeability with the hydrofracture is much larger than that of stimulated reservoir volume. Consequently, we neglect the pressure gradient within the fracture relative to the gradient in the formation.

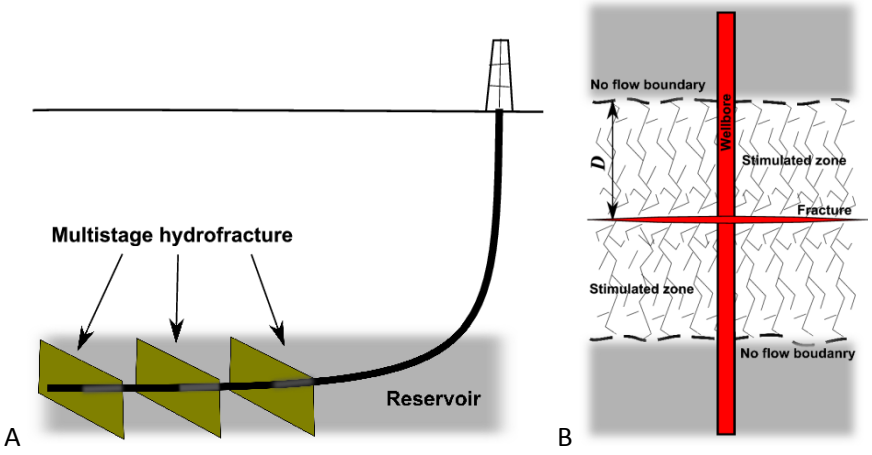

Figure 9. The flow geometry schematic in multistage-fractured gas well.

The method of integral relationships [6], see also [9], allows for obtaining an approximate solution in a simple explicit form. In heat transfer, this approach is also known as the heat balance integral method [26]. We employ the simplest first-order approximation, which is equivalent to Pirverdian's generalization of the method of evolving steady-state solutions [40]. Polubarinova-Kochina applied Pirverdian's method to model methane releases in coal mines [41]. The obtained formula expresses the gas production flow rate through reservoir parameters. The model predicts that the production decline curve will be bimodal. At early time, the pressure decline propagates into the stimulated reservoir volume not yet reaching the zero-flow boundary. During this stage, the production rate declines with reciprocal square root of time. Later, when pressure depletion reaches the boundaries of the stimulated zone, the rate declines exponentially.

Monthly production data from five Barnett Shale gas wells were used to test the model. Figure 10 shows the results of data fitting in semi-log coordinates. The lengths of time intervals where data were available are different for different wells and vary between 68 and 80 months of production. Considerable fluctuations in the data brings uncertainty in the outcome of the fitting. Nevertheless, the fitting indicates that the transition from the square-root of time production scaling to exponential decline for the analyzed wells happened after about 12 months of gas recovery operations.

To evaluate the predictive capabilities of the model, curve-fitting was applied to early data and the model-based estimates of the total production over the entire period of 87 months were compared to the measured values. Figure 11 compares the total volume of gas produced over 87 months of recovery operations with the model-based estimates based on truncated data. The horizontal axis shows the number of months of measured data used in the curve fitting. The relative errors for most ultimate recovery predictions are within 5 %. The general trend of error decline with increasing data time interval is not surprising. However, the error does not decline monotonically. This behavior can be explained by fluctuations in the monthly rates resulting, possibly, from temporary production disruptions during the respective months. For example,

such fluctuations between 10 and 20 months of production are likely responsible for the peak error in model predictions based on the first 25 and 26 months of production.

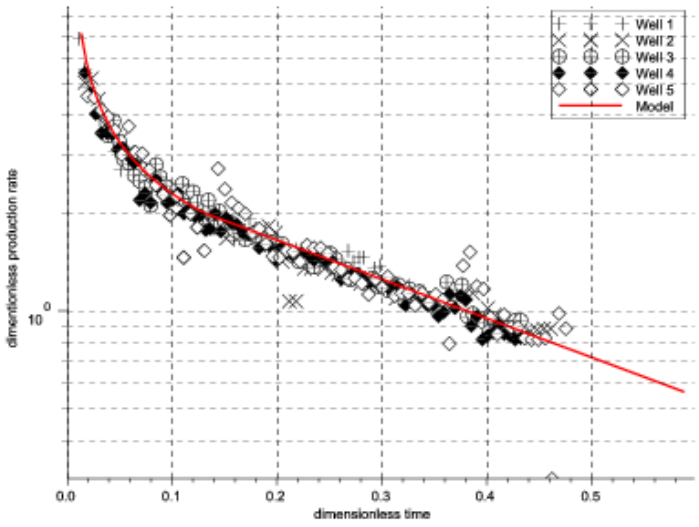

Figure 10. Data and type curve in semi-log coordinates.

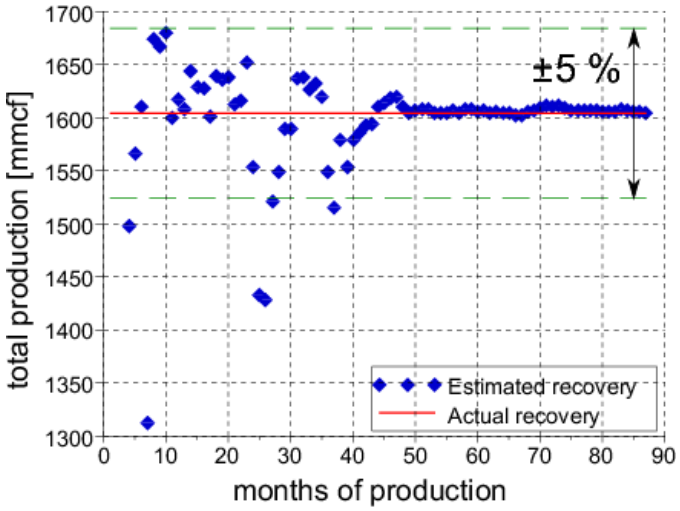

Figure 11. The diamonds show model-predicted total gas recovery over 87 months based on the number of months of production on the horizontal axis. The actual total recovery over the same 87 months is shown as a horizontal solid line. The dashed lines show ±5 % relative error range centered at the actual recovery.

We call the dimensionless quantity

$$A_S = \frac{\varrho_0 \varrho_K S_K c_f}{c_g \phi} \tag{1}$$

the adsorption storage factor (ASF). Here ϱ_0 is gas density at normal conditions, ϱ_K and S_K are the density and relative volume of the kerogen, c_f is the derivative (or, equivalently, the slope) of the adsorption isotherm, c_g is the gas compressibility and ϕ is the porosity of the rock. The ASF magnitude determines the relative contribution of adsorption gas storage. Back-of-the-envelope calculations based on FIB/SEM imaging data suggest that the magnitude of this factor can be of the order of one or higher, depending on the isotherm curve. Experimental studies of methane adsorption in shale may resolve the uncertainty related to the estimate of gas storage by adsorption.

We remark that this model is based on a number of simplifying assumptions and only can offer a reasonable first-order production data evaluation. Other factors not included in the model, like retrograde condensation or compaction, may affect gas recovery rate.

Task 5: 3D imaging of the pore space of tight sands

Objectives

The principal objective of this task is acquisition of images of tight gas sand reservoir samples at different scales. Core-scale data provides information about the presence of cracks and other heterogeneities at the scales of a faction of millimeter and higher. In addition, analysis of low-resolution CT data helps to make intelligent choices of smaller subsamples for micron-resolution tomography (micro CT). Visualization of 3D pore structure provides input data for capillary equilibrium and flow modeling (Task 7). The objective of nanometer-scale imaging to study the microporosity and very narrow slit-like pores in tight rock samples. The submicron- and nanometer-scale data, both 2D and 3D, is insufficient for direct flow simulations however. In spite of this, the images were used for developing computer-generated data, which was used for numerical experiments of Task 8.

Methods

The imaging techniques employed in this study include optical microscopy, X-ray CT, and Scanning-Electron Microscopy (SEM). Five samples denoted as Samples 1-5 were used in this study.

An optical microscope is a relative inexpensive tool for obtaining preliminary information about the grain sizes. This information helps to make an intelligent decision about the appropriate resolution and suitable sample size for micro-CT imaging.

X-ray CT images the sample interior in a non-destructive manner. CT imaging is a complex procedure involving acquisition of a large number of X-ray projections followed by a computationally intensive numerical reconstruction [27]. A stack of two-dimensional slices constitutes a 3D image. Within a slice, the data are arranged in a two-dimensional array of pixels. A pixel with the third dimension, which is the distance between two consecutive slices, is

a voxel. If a regular core is available, low-resolution CT data provide overview information about the heterogeneity and hidden damage in the core, which helps in identifying the most suitable micro-CT imaging locations. If only irregular pieces are available, the micro-CT sample selection is based on visual inspection and optical micrographs.

Visualization of 3D pore structures of tight gas sands at resolution approaching 1 micron was performed using synchrotron-based microtomography at the LBNL's ALS superbend beamline 8.3.2. The high photon flux, monochromaticity and parallel nature of the synchrotron-generated X-rays allow for considerably shorter exposure times, improved K-edge contrast imaging, higher spatial resolution, and lack of beam hardening compared to the conventional X-ray microtomography techniques. For rock microtomography, X-ray energies higher than 20 keV provided by the ALS are necessary. The mechanical and optical components of the system setup and the X-ray beam quality at ALS satisfy very stringent criteria suitable for micron-scale resolution. The LBNL team worked out an optimal balance between the maximum sample diameter and the resolution of the image suitable for the rocks of interest.

The resolution available through micro-CT imaging may be insufficient to characterize some microporosity features of a tight sand sample. Such features can be viewed with Scanning-Electron Microscopy, SEM. However, unlike X-ray tomography, the sample interior is inaccessible for SEM.

Optical microscopy

Fig. 12 shows micrographs of samples 1, 2, 4, and 5. The shapes of grains and pores are consistent with the cross-sections of micro-CT images. Note an unusual structure resembling a small droplet pending at the tip of a stem in Fig. 12 (d). The images display complex pore geometries suggesting that CT data should be at the finest resolution available at the time of imaging. The CT voxel size for samples 1, 2, 4, and 5 was 1.8 micron, and for sample 3 it was 0.9 micron. In order to run MIS and flow simulations on Samples 3 and 5, the observation resolution must be even higher, apparently of the order of 100 nm per voxel.

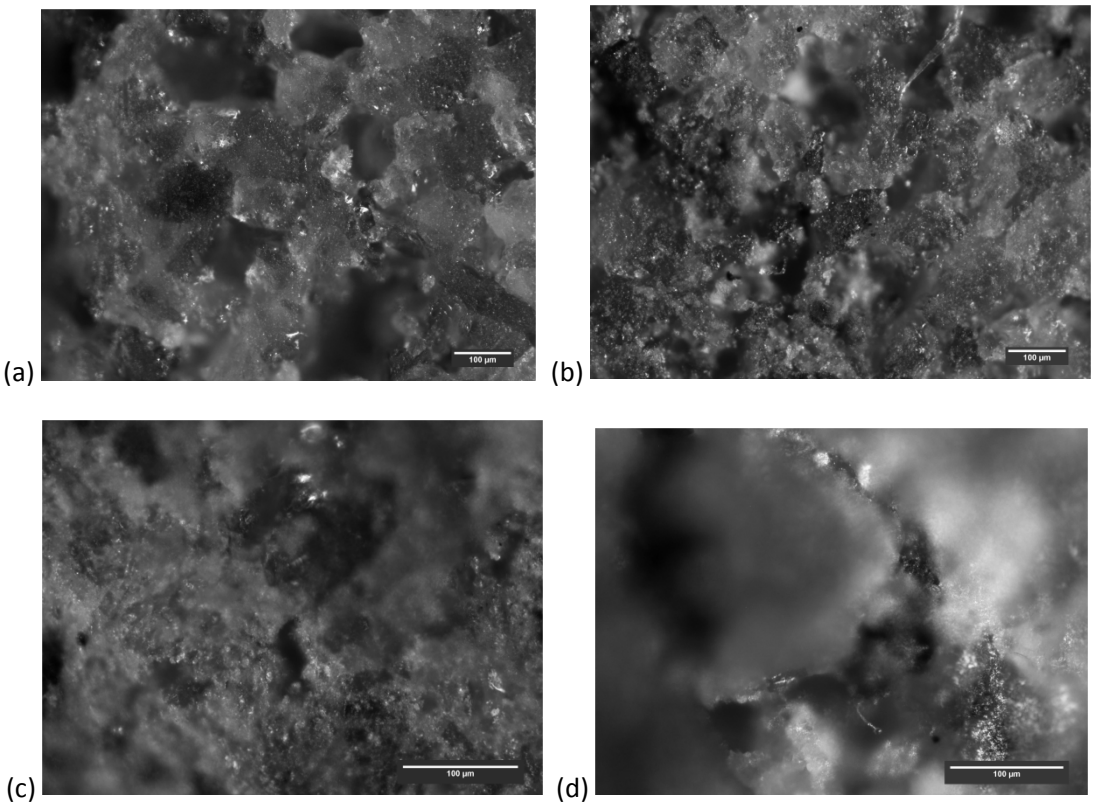

Figure 12. Micrographs of tight sand a. Sample 1, b. Sample 2, c. Sample 4, and d. Sample 5.

Low-resolution tomography

Tight sandstone samples 1–3 were photographed and then scanned using a modified Siemens Somatom HiQ medical computed tomography (CT) scanner providing 194 micron×194 micron×1000 micron voxels. Homogeneous samples of light element materials having known density were also scanned to provide a density calibration curve.

An artifact of using a polychromatic x-ray source is beam hardening [48]. Lower energy (softer) x-rays are more strongly attenuated in the outer regions of the core resulting in a brighter (higher density) appearance there. The magnitude of the beam hardening is dependent on many factors including the geometry of the scanner and core, presence of other objects in the light pathway, energy spectrum, shape of the sample, and variation and distribution of densities within the sample. For cylindrical samples having a well-distributed density variation throughout, the following technique can be effective at reducing the impact of beam hardening. The images are collected in a stack, and the stack is carefully aligned so that the circular image from each axial location is in the same location in each image. Next, the stack is viewed for large heterogeneities (crack or vein with significantly different density than the rest of the sample). If such a feature is observed, the slices containing the feature should be eliminated from the analysis. If the slices at the end of the stack contain noncircular images, they too must be eliminated. The rest of the images are then averaged along the axis resulting in a single circular image. The resulting circular image is examined for structure. The presence of significant

structure (*e.g.* off-center layers) requires reexamination of the original stack and additional modification. The averaged image is then rotated about its central axis a number of times (*e.g.* 5 rotations of 60 degrees each resulting in 6 images, each aligned but rotated 60 degrees). The stack of rotated averaged images is again averaged, and examined for structure. If the resulting rotated averaged structure is primarily only from beam hardening, the image is used further.

The minimum value from the rotated average image is then subtracted from the rotated average image, such that the values in the center of the image are approximately zero. The values will increase with increasing radius. This resulting image is then used to correct for beam hardening by subtracting it from the aligned slices. **Figs. 13** and **14** shows a result of application of this procedure. The image on the right has had beam-hardening artifacts significantly removed and, therefore, better displays sample heterogeneity. There are several flaws associated with this technique. These result from applying averages to specific densities, and from only using a small number of rotated images. Alternate approaches include obtaining the radial profile of the stack-averaged pixel values, fitting the resulting profile with a curve, creating a correction field based on this profile, and subtracting the correction field from the aligned slices. Figures 13–14 shows a result of application of the described procedure. The image on the right is free of beam-hardening artifacts visible in the picture on the left, and, therefore, better displays sample heterogeneity.

We have also developed another method to reduce the beam-hardening effect in a stack of CT images of a cylindrical core. First, the stack is carefully aligned. Next, the center of the common cross-section is identified by best-fitting of its boundary with a circle. The plot of all intensities versus the distance to the center of the circle is approximated by a cubic spline using a least-squares spline-fitting algorithm. The obtained smooth curve characterizes the average intensity associated with beam-hardening as a function of the distance from the sample axis. Further subtraction from each image voxel of the value evaluated from the distance from the voxel to the sample axis produces a relatively clean image.

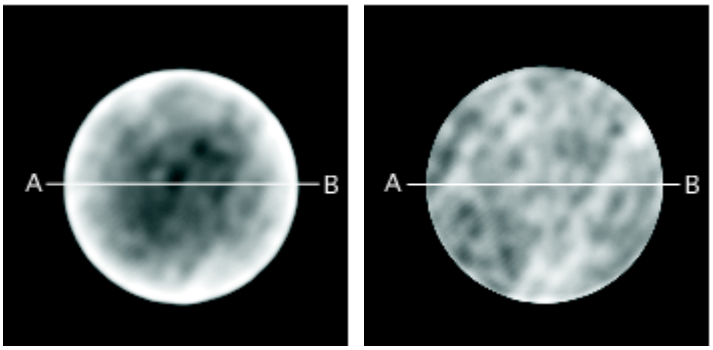

Figure 13. The original image (left), shows pixels brightening near sample boundaries, which is a beam-hardening artifact. The picture on the right shows this artifact removed.

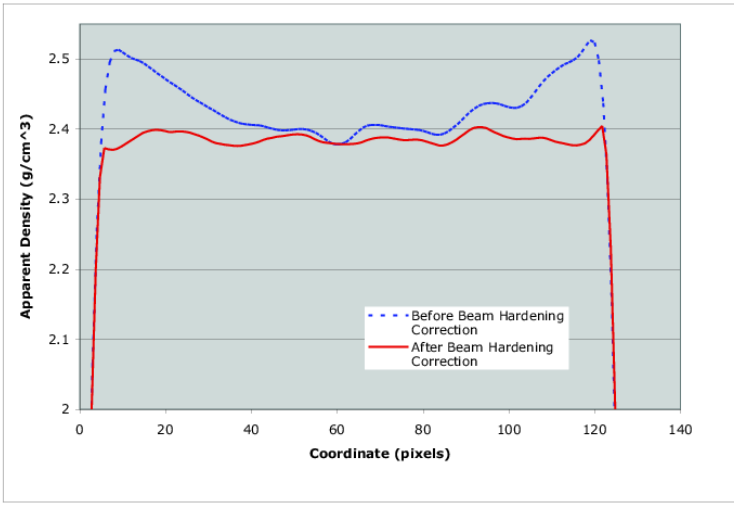

Figure 14. The intensity along the line AB, Fig. 13, before (blue dashed line) an after (red solid line) beam hardening removal shows that beam hardening can hide important features.

Photographs and cross sections from the resulting 3-D density maps are presented in **Figs. 15–17**. Three cross sectional images are shown in each of the Figures (a)–(c). These cross sections were selected because they show specific characteristics of the sample.

The most obvious visual features in Sample 1 (Fig. 15) are non-connected dark (lower density (~ 2.3 g/cm ^{3} - porosity ~ 14 % if quartz is the primary constituent) regions in the sandstone, and a high-density vein (white, density 2.45 g/cm ^{3}) present in the sample. The rock away from the vein is slightly heterogeneous, with densities ranging over 0.06 g/cm ^{3} . The rock appears to have more larger-scale heterogeneity than the other samples, and a layer of higher density material cross-cuts the sample (Fig. 15 (b)). The density of this cross-cutting feature indicates that the porosity is about 8 %, assuming quartz is the primary mineral component. The remainder of the rock has an estimated porosity of about 12 %. Fig. 16 presents results from Sample 2 which has denser and less dense layers alternating with a spacing of about 1–2 mm. This sample is a dense, well-cemented sandstone. Laminations in the rock are visible from the photograph. The CT scans also shows laminations with density differences between layers, indicating porosity of 8 % to 12 % in these contrasting layers, assuming quartz is the primary mineral constituent. Images from Sample 3 are shown in Fig. 17. This sandstone is composed of coarser grains than the other two samples, is laminated on approximately the same spatial scale as Sample 2, and contains numerous high-density grains distributed throughout the sample. The bulk density of this sample is about 2.6 g/cm ^{3} , with grain densities exceeding 2.9 g/cm ^{3} .

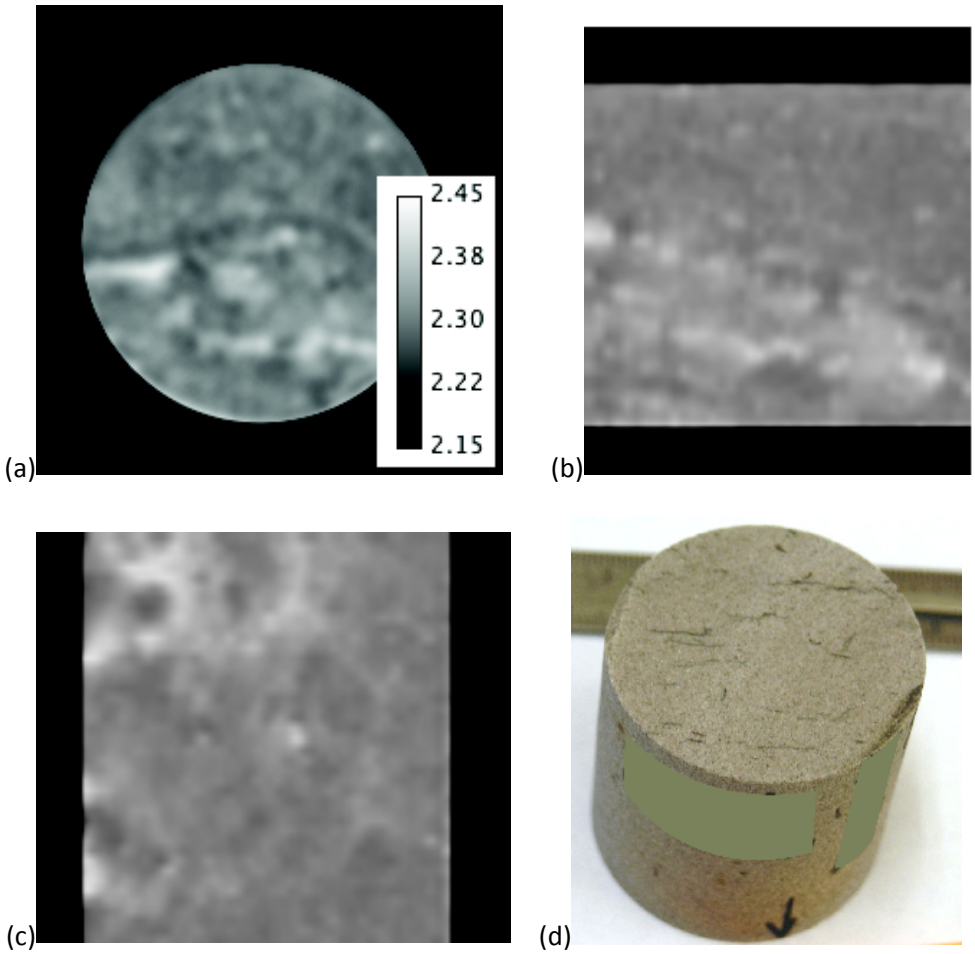

Figure 15. X-ray CT images of Sample 1 (a) axial cross section, (b) cross section along vertical central plane of (a), and (c) cross section along horizontal central cross section of (a), (d) photograph of core. The sample is 36 mm in diameter.

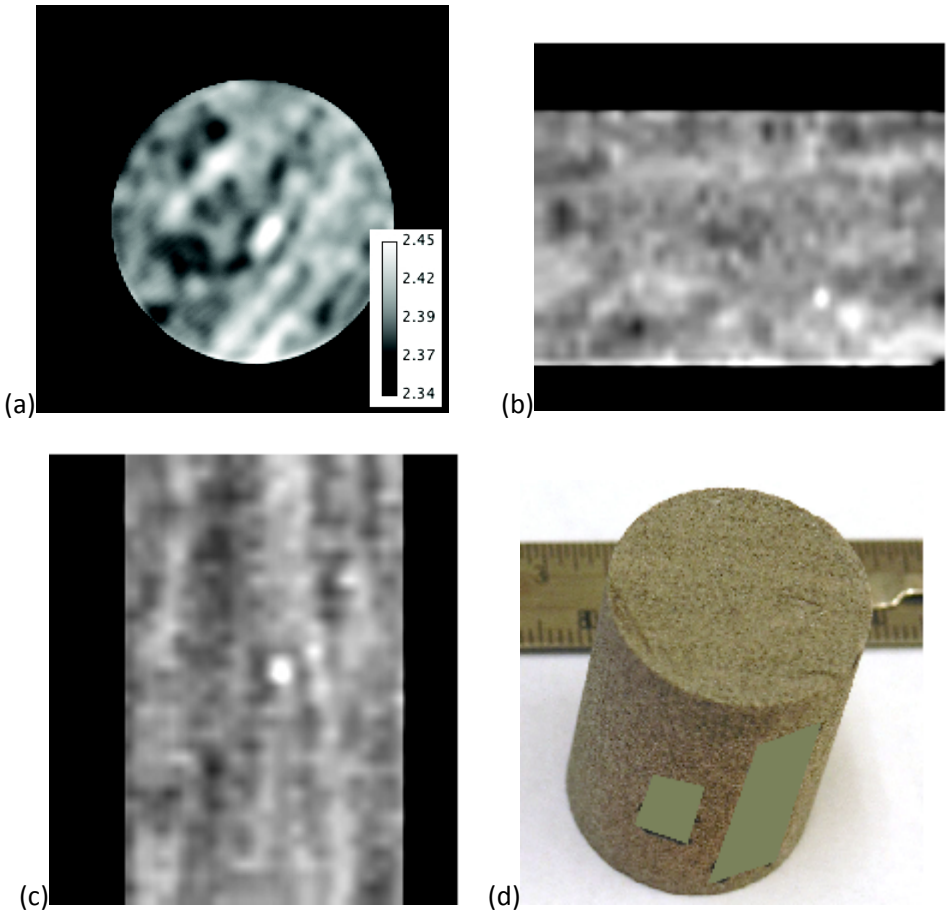

Figure 16. X-ray CT images of Sample 2: (a) axial cross section, (b) cross section along vertical central plane of (a), and (c) cross section along horizontal central cross section of (a), (d) photograph of core. The sample is 23 mm in diameter.

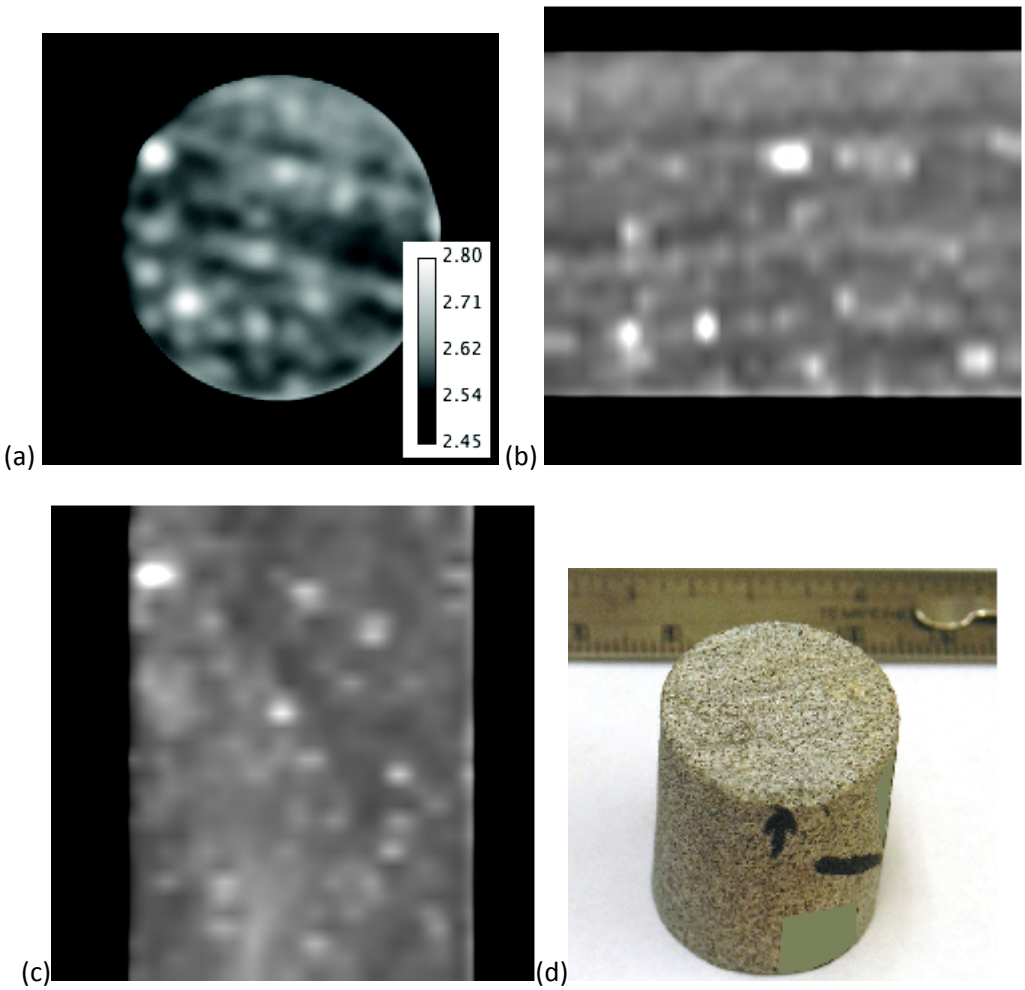

Figure 17. X-ray CT images of Sample 3: (a) axial cross section, (b) cross section along vertical central plane of (a), and (c) cross section along horizontal central cross section of (a), (d) photograph of core. The sample is 22 mm in diameter.

X-ray microtomography at the ALS

X-ray CT imaging is widely used in medicine, but it also has become a useful tool in the studies of the 3D pore structure of natural rocks [56,3,15-17]. The LBNL x-ray micro-tomography facility is based at beamline 8.3.2 at the Advanced Light Source (ALS). The setup is similar to the standard setup for this technique developed in the 1990's [30]. The x-rays are produced from a superbend magnet source and pass through a monochromator comprised of two multilayer mirrors, which can be altered in angle to select the required x-ray energy. X-ray energies from 8 KeV to 45 KeV are available. When scanning, X-ray energy was adjusted to a given total attenuation of the sample of ~1500 to 2000 arbitrary absorption units. The samples were mounted on an air bearing stage that can be adjusted in three dimensions relative to the x-ray beam. The x-rays transmitted through the sample then interact with a $CdWO_4$ single crystal scintillator that fluoresces the shadowgram x-ray image as visible light. This image was then magnified through a selection of microscope objectives and relayed onto a 4008×2672 pixel CCD camera (Cooke PCO 4000). The CCD pixel size is 9 μm, thus with a 2×, 5×, or 10×

objective a pixel size of 4.5 μm, 1.8 μm, or 0.9 μm, respectively, at the sample can be mapped onto the ccd. Due to the ccd's fixed field of view, increases in objective magnification require a proportional decrease in physical size of the sample. The maximum sample diameter is $\sim$15 mm, $\sim$6 mm, and $\sim$3 mm for the 2×, 5×, and 10× objectives, respectively. The samples were rotated in the x-ray beam from angles 0 to 180 degrees with images collected at the desired angular increment. The most common angular increment was 0.125 degrees, resulting in 1441 images as this was shown to be a good compromise point between the scan time and greater reconstructed image quality derived from collecting a greater number of raw images. Single image exposure times ranged from a minimum of several hundred microseconds to several seconds. Multiple images at a single angular location were averaged to avoid detector saturation during longer exposure times. The raw data were reconstructed using the commercial software package Octopus [20] using a filtered back projection algorithm.

SEM imaging of microporosity

In comparison to x-ray micro CT, scanning electron microscopy (SEM) is a traditional high-resolution imaging technique which uses the interaction of a focused electron beam with the sample to image features as small as 2–3 nm. Unlike micro CT, SEM is only capable of imaging sample surfaces but allows access to smaller length scales with the addition of compositional information from secondary spectroscopy measurements (*e.g.* EDS, WDS, EELS, EBSD)[1]. We utilize SEM in a supporting role to understand pore scale clay distribution. We carried out our high-resolution work using a field-emission SEM (Hitachi S-5000); for more routine tasks we used a smaller tabletop electron microscope (Hitachi TM-1000).

Fig. 18 shows a series of backscattered electron (BSE) images acquired for a small tight sandstone core depicting two different types of clay accumulation within the pores. Figure 18A shows typical stacks of pseudo-hexagonal kaolinite platelets occupying the space between two quartz grains while 17B shows less ordered montmorillonite distribution in another pore throat. Textural differences as shown in these image are difficult to resolve in micro CT imagery; the kaolinite platelets have characteristic lateral dimensions of 3–4 microns with inter-platelet spacings of less than a micron in many cases making resolution using micro CT problematic. The high surface area and variety of smaller pores present in the clays occupying spaces between sand grains will have significant impact on both permeability and gas adsorption. Unfortunately, without the use of focused ion beam methods to sequentially remove layers of the core, images of this type are limited to views of the rock surface, which is in many cases contaminated by the coring and polishing process.

[1]EDS stands for energy-dispersive X-ray spectroscopy, WDS stands for wavelength dispersive spectroscopy, EELS stands for electron energy loss spectroscopy, and EBSD stands for Electron Back Scatter Diffraction.

Fig. 19 shows a comparison of a micro CT slice and an surface SEM image for the same core. From a flow modeling perspective, a micro CT slice (1.8 microns thick) provides a better planar cross-section. However, the contrast limitations in micro CT make segmenting quartz grains from clay fill difficult if only intensity is used in the analysis process. While SEM is limited to a surface image, the texture of the filling clay is readily apparent.

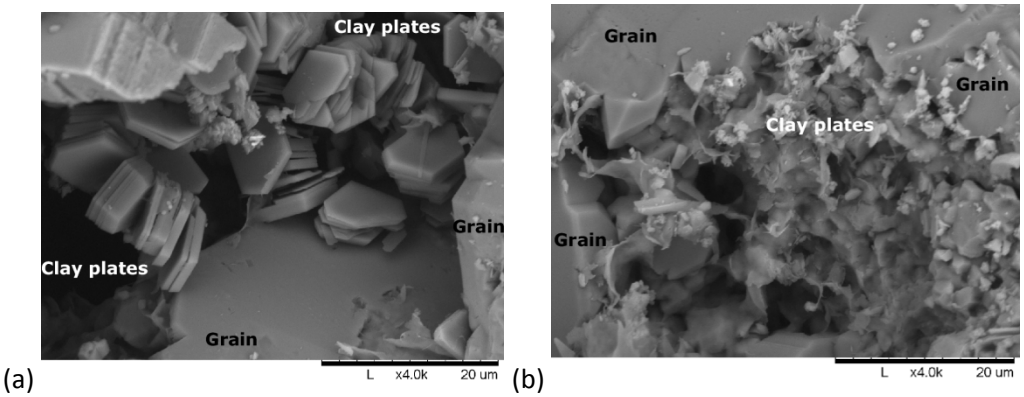

Figure 18. SEM 4000x magnification images show different types of clay plates contribute to the microporosity of the sample: kaolinite (a) and montmorillonite (b).

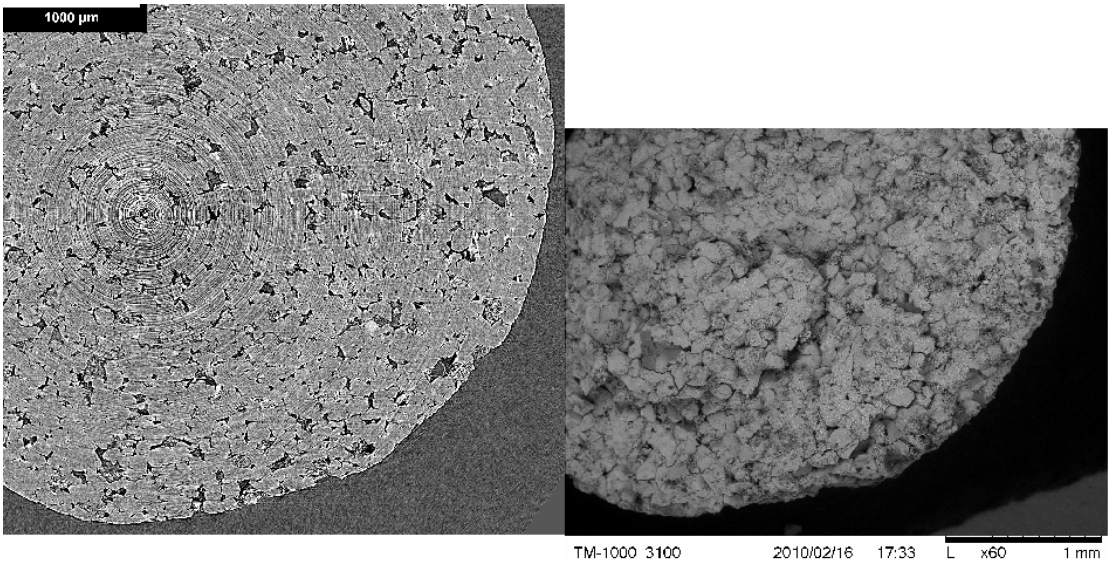

Figure 19. A micro CT reconstruction, on the left, accurately reproduces a planar cross-section of a sample, whereas a SEM image, on the right displays the rough surface of the sample.

Submicron-resolution tomography

The pores in some tight-sand samples were so small that micro CT imaging at the ALS was insufficient to resolve pore geometry. Xradia, Inc., a manufacturer of high-resolution tomography tools, kindly offered to acquire 500-nanometers resolution images of a tight gas sample. The scan was made on a VersaXRM 500 machine at Xradia facility in Pleasanton, CA. The selected sample had extremely narrow pores and low porosity. Micro-tomography imaging of such a sample is challenging. The quality of the Xradia VersaXRM 500 results was amazing. The

high image contrast is very important for multi-phase image segmentation, The noise and artifacts were practically unnoticeable. Figure 20 shows a 2D slice of Xradia micro CT data, whereas Figure 21 shows a 3D reconstruction. Both examples show high contrast and low level of noise.

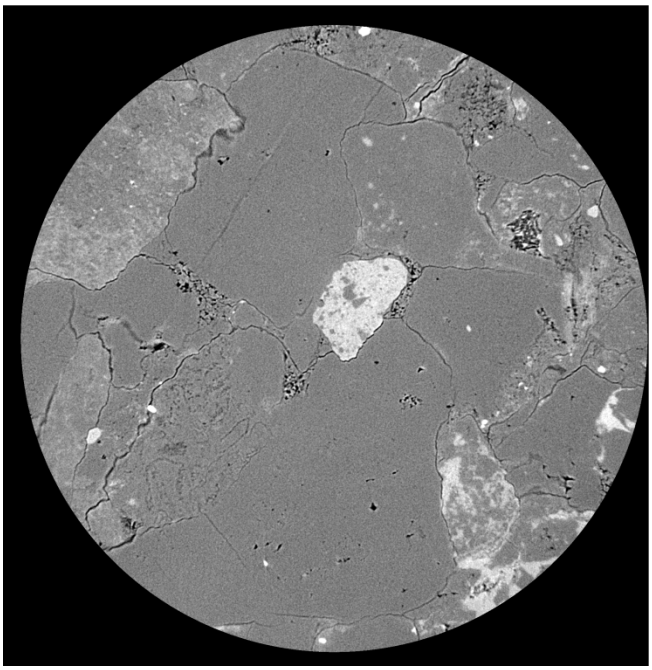

Figure 20. A slice of microtomgraphy data at 500 nm resolution shows high contrast and very low level of noise. The image is courtesy of Xradia, Inc.

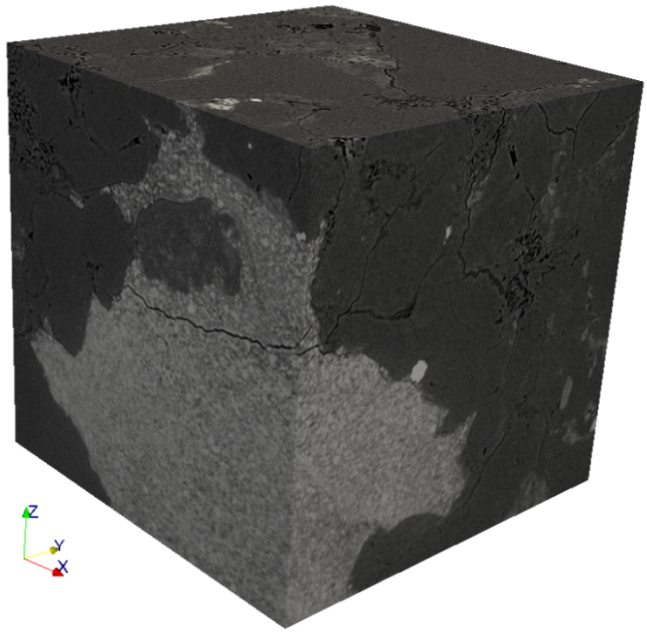

Figure 21. A 0.5x 0.5x 0.5 mm tight-sand sample at 500 nm resolution. Micro CT data are courtesy of Xradia, Inc.

Results and Discussions

The five samples used in this study are denoted “1” through “5”. The term “tight sand” is not rigorously defined. One of the definitions is sands requiring well stimulation for gas production. At the grain-scale level, tight sands are usually densely packed small grains. **Fig. 22** (a), shows CT cross-sections of a conventional sandstone sample, compared to a tight-sand sample in Fig. 22 (b). Note that even though the grain sizes and shapes do not differ dramatically, the porosity of a tight-sand sample is dramatically smaller than that of the conventional sand and some pores are filled.

(a) 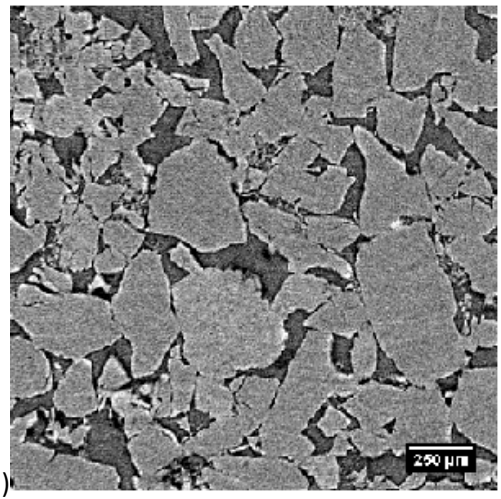

(b) 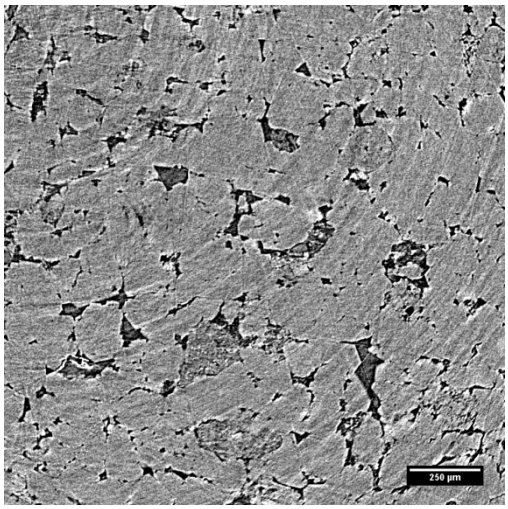

Figure 22. Two-dimensional cross-sections of micro-CT images of conventional outcrop sandstone (a) and tight sand (b) samples at resolutions of 4.5 and 1.8 microns, respectively.

The small porosity creates difficulties in image reconstruction and segmentation. Additionally, the pores are frequently filled with clay particles whose dimensions are much smaller than those of the grains, see Fig. 18. The tight sand image in Fig. 22 (b) (sample 1) is compared with images of the other samples, samples 2, 3, 4, and 5 in **Fig. 23**. The densely packed grains in samples 3 and 4 leave almost no porosity. The lighter colors in the images indicate a higher material density. The quartz grains are dark-gray in color. The images were acquired at the Advanced Light Source x-ray microtomography facility at different times. The facility upgrades resulted in higher quality and higher resolution image of sample 3. The concentric rings noticeable in the gray-scale images, Figs. 22 (b) and 23, are computed tomography image reconstruction artifacts [32].

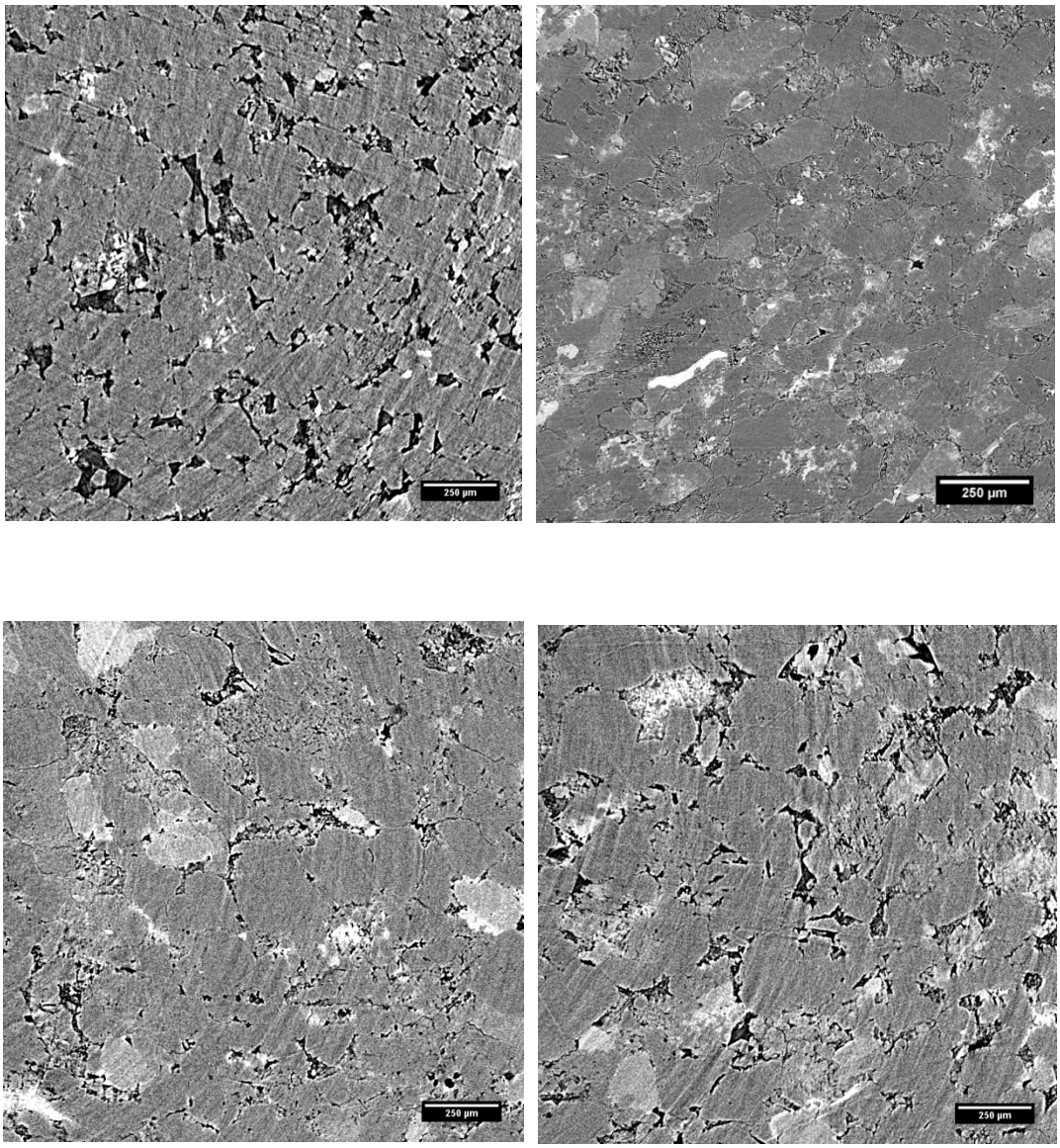

Figure 23. Two-dimensional cross-sections of micro-CT images of tight sand samples. Voxel size is 1.8 microns, except the top right image, where the voxel size is 0.9 micron. The samples are numbered 2–5 row-wise, starting from the top left image.

Fig. 24 shows volume and orthoslice views of a three-dimensional reconstruction of a tight sand sample. The noticeable slit-like few micron wide pores make modeling and simulation very challenging.

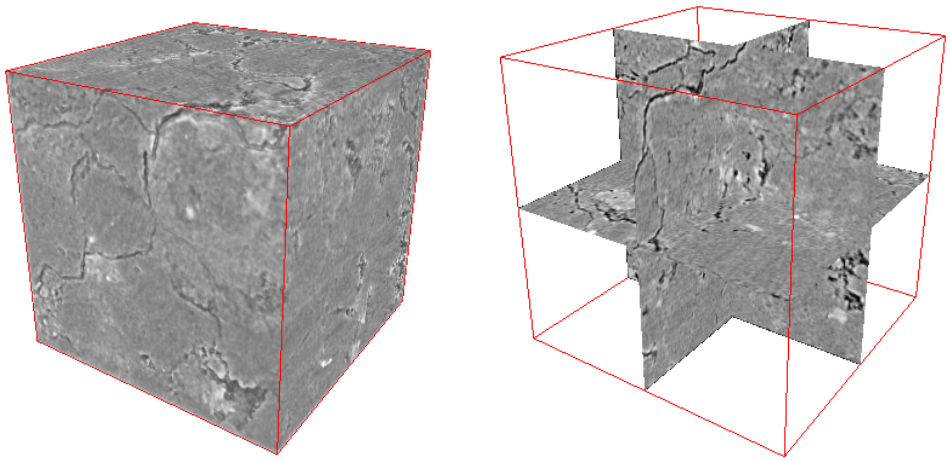

Figure 24. A 3D reconstruction of a tight sand sample of dimensions 0.7 mm^3. Narrow, just a few microns, slit-like pores result in a very low permeability and make simulations very challenging task.

All samples in this study have complex pore geometry. For some samples, the pore geometry was reconstructed sufficiently well for further modeling of two-phase flow properties. Simulations predict that a relatively small amount of the wetting liquid, whether it is brine or gas condensate, may trap gas thus making it disconnected. MIS calculations in combination with flow simulations suggest an interpretation of the "Permeability Jail" phenomenon [47,14]. In imbibition, the non-wetting gas phase becomes disconnected and thus immobile by capillary forces. Since the amount of the wetting liquid that causes the gas phase disconnection is small, the respective liquid saturation is insufficient for developing appreciable mobility. Thus, both fluids become effectively blocked by each other.

Resolution gap

A general conclusion suggested by micro CT and modeling studies of tight sand samples is that the major difficulty is reconciliation between different scales. On one hand, the grain size is of the order of hundreds of microns. It means that the study volume dimensions must be also at least of the order of hundreds microns. At the same time, some pores are filled with clay particles, and some pores are slit-like openings of submicron aperture, see Figure 25. Image resolution for detection and visualization of such microporosity features must be of the order of nanometers. The grain size makes FIB/SEM imaging for tight sands inefficient. The pixel size of computed tomography images usually does not go below 0.5 micron. There is a gap between nanometer resolution of SEM data and micron resolution of tomography data yet to be filled. Xradia is developing new tools which are supposed to fill this gap, and there is a nanotomogrpahy facility at the Advanced Photon Source at Argonne National Laboratory [19]. However, tool resolution is not the only problem. The requirements to sample size for nanotomography are very stringent and cutting a sample should be done with a laser ablation tool. An attempt of shale nanotomography did not succeed within this project due to the sample preparation and mounting issues. These difficulties make tight sand nanotomography unfeasible at this time. An alternative approach is pore-scale simulations on computer-generated data

mimicking the geometry of tight sand samples observed in SEM and micro CT data, as described in Task 8.

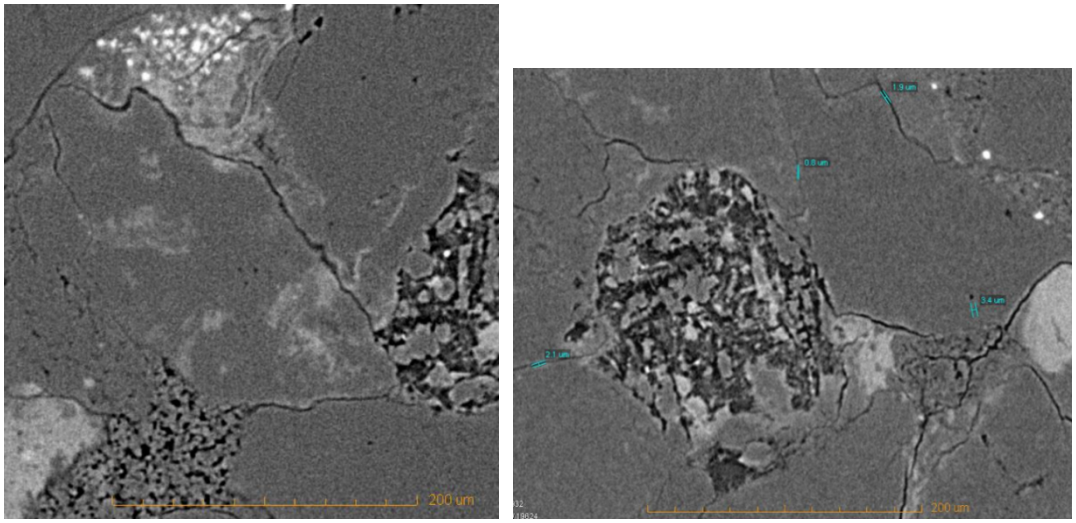

A B

Figure 25. Clay filling of pores and submicron aperture slit-like pores in tight gas sand. The images are courtesy of Xradia, Inc.

Task 6: A model of retrograde condensation at the matrix-fracture interface

Objectives

Besides methane, natural gas composition may include many other hydrocarbons and non hydrocarbon compounds [37]. Depending on the pressure and temperature conditions, these other compounds may be present in gas or liquid phases, or both. Natural gas is called wet or dry depending on the liquefiable portion of gas composition. The equilibrium distribution of each component between the gas and liquid phases is determined by equality of their chemical potentials. Figure 26 adapted from [39] shows a representation of a phase diagram of a reservoir hydrocarbon mixture. Consider a scenario where the diamond denotes the initial reservoir pressure and temperature conditions. Pressure depletion will move the pressure–temperature point downwards, towards the shaded zone in which some hydrocarbon components will dropout as liquid from the gas mixture. This phenomenon is called retrograde condensation. As the pressure further depletes, the liquid condensate may vaporize through secondary evaporation [37].

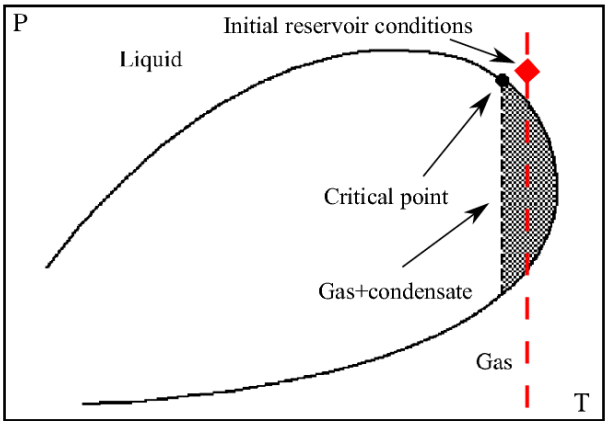

Figure 26. Phase diagram of hydrocarbon mixture(modified from[39]). The shaded zone denotes gas-condensate system, the dashed line corresponds to the reservoir temperature, and the diamond denotes the initial reservoir conditions.

The objective of Task 6 is development of a model of retrograde condensation at the interface between low-permeability matrix and a fracture. This was upscaled to the reservoir scale and compared to existing models [37,34] with good agreement. The model was apply to an optimal-control problem of maximizing the total gas production at a fractured gas-condensate well with dynamic liquid skin.

Methods

The model assumes thermodynamic equilibrium. In pores, the flow is governed by Stokes equations, and the flow is assumed to be steady. We further assume that no significant cooling or heating takes place, so that the density of the wet gas mixture, ρ_g, is a function of pressure only: $\varrho_g = \varrho_g(p)$. Wet gas is the sum of the dry component that remains in gas phase within the pressure range of interest, and the liquefiable component, which is in the gas phase at the beginning, but may drop out as liquid if the pressure drops sufficiently, see [1]. Let c denote the mass fraction of the liquefiable gas phase in the wet gas composition at thermodynamic equilibrium. Concentration c is a lumped quantity. A real gas mixture is multicomponent and each component concentration depends on all other concentrations. The lumped concentration, c, depends on the initial wet gas mixture composition, the history of pressure depletion, and the properties of the mixture and components. Under isothermal conditions, c is a function of pressure only: $c = c(p)$. There is a certain arbitrariness in defining c.

The optimization problem is solved using a gradient descent method [25]. Evaluation of the gradient employs a solution to the adjoint system [42]. Although this approach requires additional analytical calculations, it makes the numerical procedure much more efficient.

Results and Discussions

Let $\mathbf{u}_g$ be the local velocity of steady flow of wet gas in the pores. The local rate of the liquid condensate, Q_{lc}, dropout is given by equation

$$Q_{lc} = \frac{d}{dp}\left(c(p)\varrho_g(p)\right)\nabla p \cdot \mathbf{u}_g \tag{2}$$

Note that the pressure gradient is not necessarily parallel to the local flow velocity vector. To estimate the rate of liquid accumulation in a certain volume of the rock, the local rate in Equation (2) must be integrated over the pores inside this volume. Such an integration upscales the model. Cumbersome but straightforward calculations involving the Green–Gauss–Ostrogradsky divergence theorem [36] yield that at the Darcy flow scale the rate of liquid dropout is proportional the pressure gradient squared [53]. This conclusion is in agreement with the relation derived by others [37,34,39]. Thus, for the liquid saturation, S, one obtains

$$\phi\varrho_c\frac{\partial S}{\partial t} = \frac{d}{dp}\left(c(p)\varrho_g(p)\right)\frac{k_{rg}(S)k}{\mu_g}\varrho_g\nabla p\cdot\nabla p \tag{3}$$

Here $k_{rg}(S)$ is the relative permeability to gas, k is the absolute permeability of the rock, and μ_g denotes gas viscosity.

Due to higher permeability, the pressure in the fractures is lower than that in the matrix blocks. Inside a matrix block surrounded by low pore pressure fractures the pressure gradient is distributed very nonuniformly. The sharpest pressure drop occurs at the matrix-fracture interface. By virtue of Equation (3), the most intensive liquid condensate accumulation is an a thin layer at this interface. Moreover, a higher rate of liquid accumulation means a higher decline rate for the permeability to gas. Lower permeability results in an even higher pressure gradient relative to the inner part of the porous block. Thus, the gas permeability reduction has as elf-accelerating feedback effect: the lower permeability results in a higher pressure gradient, which yields relatively higher liquid dropout rate, which further reduces the permeability to gas. Following [8,7], we assume that retrograde condensation forms a thin skin at the matrix-fracture interface, shown schematically in Figure 27.

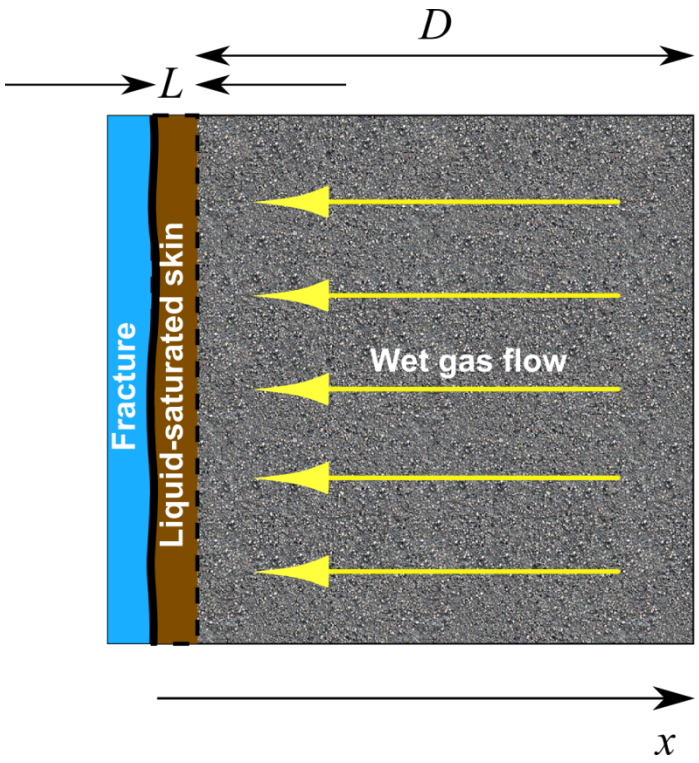

Figure 27. A schematic of liquid-saturated skin at matrix-fracture interface

The dynamic-liquid-skin gas flow model suggests that if the pressure in the fracture is maintained low, the initially high flow rate will be followed by rapid decline due to early skin buildup. If the pressure control would maintain fracture pressure high, the liquid skin will accumulate slowly, but the production rate also will be low. A natural question to ask is if there is optimum pressure control regulating the flow rate in such a way that the total gas recovery over a given period of time will be maximized. It turns out that the answer is yes. The solid line in Figure 28 plots the estimated recovery a function fracture pressure squared in dimensionless units. The solid line is evaluated assuming that the fracture pressure is constant in time. This plot shows that a too-low pressure may result in poor performance from the point of view of ultimate recovery. The reason is early liquid-condensate skin development due to high pressure gradient. A too-high pressure does not result in liquid skin buildup. However, it also results in poor performance due to the slow flow. However, the optimal time-dependent pressure control yields yet a larger recovery estimate. The optimal recovery is shown in Figure 28 as horizontal dashed line. It outperforms the best constant-pressure control by about 20 % of the recovery volume. In the optimal pressure regulation regime, the flow rate is close to constant over the entire period of time.

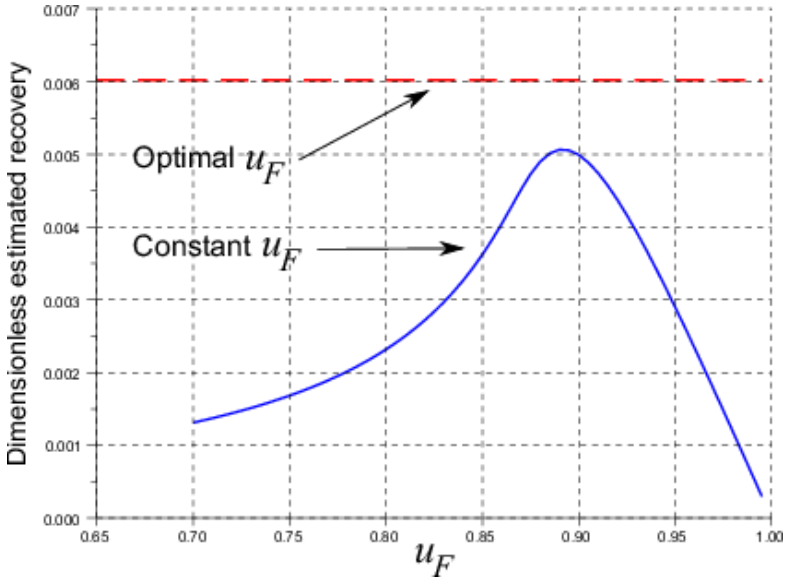

Figure 28. Evaluation of dimensionless estimated ultimate recovery as a function of u_f shows strong impact of fracture pressure. The optimal recovery estimate exceeds the best constant-pressure result by approximately 20 %.

More technical details related to Task 6 can be found in [53].

Task 7: Prediction of petrophysical rock properties form pore space geometry

The main effort of this task was the tevelopment and implementation of methods and algorithms of numerical evaluation of rock flow properties from segmented micro CT data.

Subtask 7.1. Modeling Klinkenberg effect: flow with slippage

Objectives

The Klinkenberg effect [31] is dependence of gas permeability on mean gas pressure. The objective of this subtask is development of pore-scale numerical model for simulating flow with slippage. Simulations were used to plot correlations between Klinkenberg coefficient and the estimated Darcy permeability.

Methods

To account for the Klinkenberg effect, new slip boundary conditions at the pore walls were introduced into pore-level flow models and simulations. Analytical calculations estimate the correlation between flow conductivity and slippage for channels of simple geometries. For more complex pore geometries, evaluation of permeability was conducted numerically. First, in order to reduce the dimensionality of finite-difference equations, dead-end clusters are detected and removed from the computational domain. After that, Stokes flow equations are solved and average flow is used to evaluate the permeability.

Results and Discussions

One of the differences between liquid and gas states of matter is that in gas molecules are packed less densely. The molecules move around with a speed determined by the temperature and collide with each other. The average distance travelled by a molecule between collisions is called mean free path. In ideal gas, the mean free path is infinite. Ideal gas can be a reasonable model for relatively low pressures. However, as the density of the gas grows with increasing pressure, the molecules collide more frequently and the ideal gas model becomes inadequate. The average number of collisions experienced by a molecule per unit time, Γ, is given by

$$\Gamma = \xi' n\pi\sigma^2\Omega \tag{4}$$

where n is the number of molecules in a unit volume, σ is the molecular diameter, and Ω is the mean velocity. This formula is based on a spherical model of a molecule [28]. The effective radius, σ, is of the order of 10 Å□, where 1 Å□ $=10^{-10}$ m. The predicted value of the dimensionless parameter ξ' is different depending on the statistical model of the distribution of velocities. For the Maxwellian distribution, $\xi' = \sqrt{2}$. The mean velocity for this distribution equals

$$\Omega = \sqrt{\frac{8\pi}{mkT}} \tag{5}$$

where T is the absolute temperature, m is the molecular mass, and k is the Boltzmann constant: $k = 1.3806503\times10^{-23}$ JK^{-1}.

At a given temperature, the frequency of collisions between the molecules can be characterized by mean free path, l. Clearly, $\Gamma = \Omega / l$. Thus,

$$l = \frac{1}{\xi' n\pi\sigma^2} \tag{6}$$

From the ideal gas equation of state, $p = nkT$, where p is the gas pressure. Thus, for the ideal gas model,

$$l = \frac{kT}{\xi' p\pi\sigma^2} \tag{7}$$

In other words, at a fixed temperature, the mean free path is inversely proportional to the pressure.

For example, assume a 1 km (~3300 ft.) deep reservoir with pore pressure of 100 atm ($\approx$ 1500 psi) at a temperature near 400 K (~260 F). A substitution of the numbers yields a mean free path estimate at $l \approx$ 1.24 Å□.

The redistribution of the gas molecules concentration by diffusion is not a part of the dynamic flow covered by Navier–Stokes equations. So the total gas flow is a superposition of both. Normally, the diffusion component of flow is negligible relative to the dynamic flow. However, it may be not so if the domain where the flow occurs is small enough, so that its linear dimensions are comparable with the mean free path. The coefficient D of molecular self-diffusion, that is redistribution of the gas molecules due to the gradient of concentration of the molecules, ∇n, also can be expressed through the mean free path and mean velocity:

$$D = \frac{1}{3} l\Omega = \frac{\Omega}{3\xi' n\pi\sigma^2} \tag{8}$$

In particular, the coefficient of diffusion depends on concentration.

The Knudsen number

$$\mathrm{Kn} = \frac{l}{L} = \frac{1}{\xi' n\pi\sigma^2 L} \tag{9}$$

is a dimensionless ratio of the mean free path, l, to a characteristic length scale, L. Its magnitude is used as a criterion for transition between different flow regimes. If Kn is between 10^{-3} and 10^{-1}, then slippage at the pore walls needs to be taken into account [45,5].

The molecular density n in Equation (9) is a function of pressure. The gas in reservoir conditions is stored compressed, and the magnitude of Knudsen number may be not as large as in rarefied gas flow. Some recent studies mention an alternative to Maxwell's slippage mechanisms. For example, the wettability can play a role [59,60]. Natural rocks usually are not gas-wet, that is, it is more likely that the solid grains will establish a direct contact with any reservoir fluid, but gas. Although it is not the case for kerogen inclusions capable to adsorb methane molecules [22,23,44,55,10,11], in tight sands the gas most likely flows in pores with walls or pores covered by a wetting-liquid film, which would serve as a lubricant. To summarize, the physics of slippage in gas flow may need further theoretical and experimental study.

Boundary condition

In liquid flow, the liquid molecules stick to the bounding walls implying no-slip boundary conditions [33]. Ideal elastic collisions between gas molecules and an ideal smooth surface result in no energy loss. The molecules merely bounce from the walls imposing no shear stress on the bulk gas flow. However a real surface is not smooth, which needs to be taken into account for adequate modeling. Maxwell [35] derived partial slip boundary conditions for gas from the kinetic theory. In partial slip, the tangential component of gas velocity, v_τ, near the wall satisfies the following relationship:

$$v_\tau = G\frac{\partial v_\tau}{\partial n} \tag{10}$$

where G is the slip factor and $\partial / \partial n$ denotes the normal derivative. Some generalizations of condition (10) resulted in higher-order slip conditions [18] and slip conditions in a tensorial form for a case where the surface roughness is anisotropic [61].

Although Maxwell's condition was originally derived for flow of rarefied gas, it is applied to flow in a micro-channel as well [5]. According to Maxwell's theory of gas slip, some gas molecules hit and bounce off the wall in an elastic manners. These molecules preserve the mean tangential component of velocity v_τ. However a fraction of molecules, denoted by f, $0 < f < 1$, experiences multiple collisions with the wall due to its roughness. These molecules eventually bounce off from the wall, but they lose the tangential component of the velocity due to multiple collisions. The wall adsorbs the tangential component of the velocity. In experiments, the magnitude of f was found between 0.2 and 1, where the lower boundary $f = 0.2$ corresponds to a very smooth wall. Calculations yield the following formula for the slip factor:

$$G = \frac{2}{3}\left(\frac{2}{f} - 1\right) l \tag{11}$$

see [35].

For some simple geometries, viscous flows with slip boundary conditions can be characterized by explicit formulas. For example, equation

$$f_x = -\frac{L^2}{12\mu}\left(1 + \frac{G}{L}\right)\frac{\partial p}{\partial x} \tag{12}$$

expresses the volumetric flux in direction x, f_x, in viscous flow between two parallel planes separated by a distance L.

For viscous flow in a cylindrical capillary tube of radius R, the flux is expressed as

$$f_x = -\frac{1}{8}\frac{1}{\mu}\frac{\partial p}{\partial x} R^2 \left(1 + 4\frac{G}{R}\right) \tag{13}$$

The proportionality between the volumetric flux and pressure gradient characterizes the permeability. Equations (12) and (13) suggest that in simple geometries, such the correlation between permeability and slippage is linear. It is not the case for more complex geometries, where this correlation was studied numerically. Figure 29 shows results of flow simulation with slippage boundary conditions. The input data were computer-generated samples: a sample mimicking sandstone with crack, a sample modeling sandstone matrix, and a sample with slit-like pores, or fractures. The results show that the dependence of the permeability on slippage factor is qualitatively similar in all situations. The sample with crack, though shows slow

permeability increment. The distinctive feature of this sample relative to the other two is permeability contrast: fracture carries most of fluid flow. Unlike flow in simple-geometry channels, where the correlation between the flux and slippage is linear (see Equations (12) and (13)), the computations predict nonlinear dependence of the permeability on slippage.

The slippage coefficient G is defined in Equation (11). It has the dimensionality of length. An accurate evaluation of this coefficient in specific physical conditions needs further study. The algorithms developed are ready to accommodate the specific value of G as input parameter.

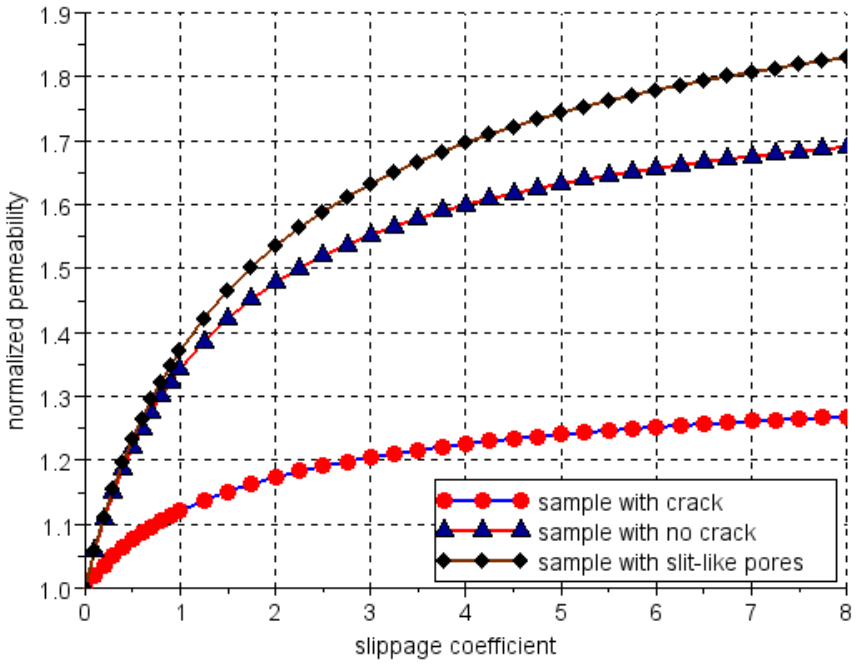

Figure 29. Estimated permeability versus slippage coefficient. The permeability is normalized with no-slip flow.

Subtask 7.2. Two-phase flow properties: the MIS method

Objectives

The principal objective of this subtask is to develop methods and tools for numerical evaluation of two-phase capillary pressure and relative permeability curves for tight rocks. Segmented 3D micro CT images of tight rock samples, Task 5, describe the pore-space geometry and are used as input data in numerical simulations. This digital-rock approach complements core-laboratory experiments which are especially time-consuming and prone to uncertainty for tight-rock cores. Digital-rock methods can be used for rock characterization or for reduction of uncertainties in reservoir models [38,43,46].

Methods

Two methods were developed within this subtask: the method of maximal inscribed spheres (MIS) and numerical simulations of creeping viscous flow in pores by solving Stokes equations.

The method of maximal inscribed spheres

The method of maximal inscribed spheres simulates capillary equilibrium fluid distribution in the pores. Its capability to predict fluid distribution and capillary pressure curve have been verified against experimental data [54,49,58]. The idea is simple. For a given capillary pressure p_c, one seeks the part of the pore space that can be covered by spheres of the radii equal to or greater than the radius determined by p_c through the Young–Laplace equation. The portion of the pore space determined this way is occupied by the nonwetting fluid. The complementary part of the pore space is, respectively, occupied by the wetting fluid, and its relative volume determines the value of saturation. The plot of saturations versus p_c, obtained in this manner, defines a computed capillary pressure curve. Figure 30 schematically illustrates the idea.

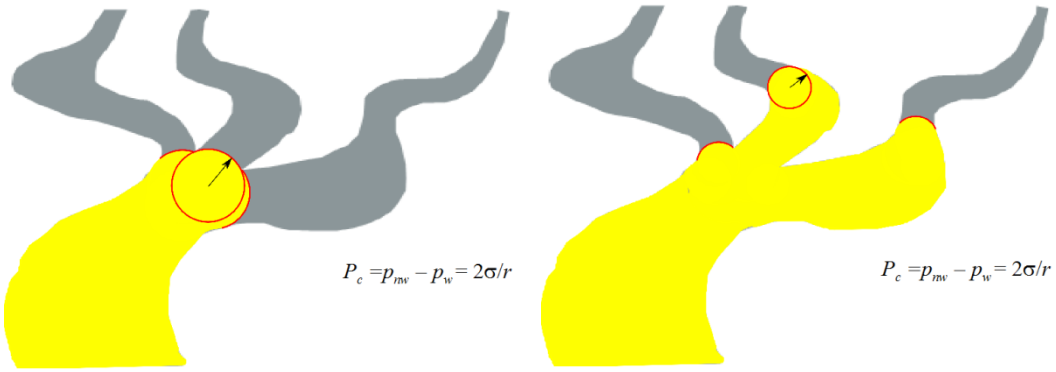

Figure 30. A schematic 2D illustration of the method of maximal inscribed spheres: The area swept by inscribed spheres of a given radius determines the part of the pore space occupied by the nonwetting fluid. The radius decreases at increasing capillary pressure. The picture in Exhibit A corresponds to a capillary pressure lower than that in exhibit B.

The key operation in this procedure is the determination of relative volume. Its implementation into an algorithm and computer code can be done independent of capillary pressure, in dimensionless units. The respective capillary pressure is dimensionless, but can be converted into physical units using the image resolution (voxel size) and the coefficient of surface tension. MIS calculations can model different quasi-static fluid displacement scenarios where the process is presented as a sequence of equilibrium configurations. For example, drainage displacement can be modeled by accounting only for the nonwetting phase saturation connected to the boundaries. Drainage displacement can be modeled with an invasion percolation algorithm involving cluster search methods [49]. Ordinary percolation is more suitable for modeling a two-phase fluid distribution resulting either from gas exsolution or liquid dropout, where the presence of fluid phases is the consequence of local thermodynamic equilibrium rather than fluid displacement by flow.

To handle binary digital data, the spheres have to be discretized. The shape of a small radius sphere discretization only remotely resembles an ideal round sphere. Fluid distribution at high capillary pressure is likely to be affected by microporosity, which is frequently beyond the resolution of imaging tools. Thus, the capillary pressure predictions for low wetting fluid saturation are less reliable than for medium and high saturations. In addition, the MIS-calculated fluid-fluid interface can be only considered as an first-order approximation to the complex geometry of real interfaces. Nevertheless, analysis of the pore geometry of a FIB/SEM scanned sample of chalk produced results which are in good agreement with experimental data [58]. Chalk also has very small pores. Moreover, MIS-calculated fluid distribution can mimic fluid distribution obtained by micro CT imaging [54]. Figure 31 A shows fluid distribution in a CO_2 flood experiment imaged by Jonathan Ajo-Franklin at the Advanced Light Source facility of LBNL. Figure 31 B shows fluid distribution predicted by MIS calculations. The MIS calculations simulated drainage displacement with the direction of flow aligned with the core orientation in the experiment. Although there is no rigorous one-to-one correspondence between the experimental and computed fluid distributions, there are strong similarities between exhibits A and B of Figure 31.

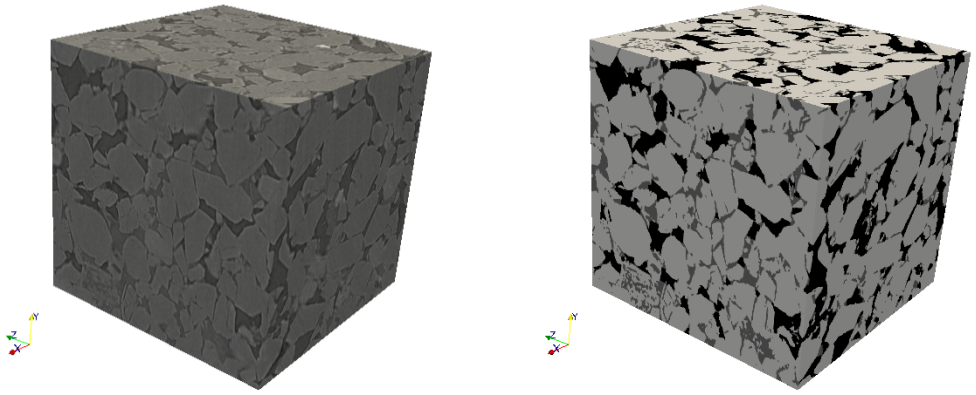

A B

Figure 31. Gray-scale micro CT image (A) and MIS calculated two-phase fluid distribution in a 2 x 2 x 2 mm^3 sample of sandstone. The 4.5 µm resolution CT data were acquired by Jonathan Ajo-Franklin at the Advanced Light Source facility of LBNL.

Evaluation of permeability and relative permeability curves

Permeability is estimated by solving Stokes equations of viscous flow followed by averaging the flow field. The domain for numerical simulations is naturally derived from a segmented 3D micro CT image of a rock sample. The inlet and outlet boundary conditions for pressures mimic pressure gradient. The computed mean flux estimates Darcy velocity. In this study, we employ finite-difference discretization of the Stokes equations. This choice was motivated by the capability of finite difference discretization to rigorously account for the boundary conditions, including both slip and no-slip conditions at the pore walls. We implement customized

modifications of the two methods by A.Chorin [12,13] to simulate flow in three orthogonal directions, and estimate the permeability tensor by averaging the flows. Sparse matrix library [21] was employed for solving linear systems of equations.

Solution of flow equations is a very computationally intensive task. To reduce the computational complexity of the problem, we have developed a dead-end clusters search algorithm. This algorithm identifies clusters of voxels in a digital image which form pockets with zero through flow. Such clusters are detected prior to solving the flow problem on the entire domain. Since the flow in such clusters is zero and does not affect the permeability estimate, they can be safely eliminated from the computational domain.

The work of the algorithm can be illustrated using two examples. Figure 32 shows two examples of such dead-end clusters in two dimensions. The solid voxels are dashed and the pores are blank, whereas the bold solid line marks the pore-solid boundary. In Exhibit A, voxel a is connected to rest of the pores only through two faces: on the left and on the right. The pore voxels to the right from voxel a are mutually connected, and voxel a provides the only channel connecting this cluster to the rest of the pore space. In discretized steady flow, the velocities on all faces of voxel a are zero. Indeed, the right-hand face velocity must be zero since otherwise the fluid would accumulate in the cluster. One the left-hand side face, the velocity also must be zero since otherwise there would be fluid accumulation in voxel a. The zero velocity at the right-hand face of voxel a implies zero velocity in the entire cluster. Thus, the system of equations can be reduced by elimination of voxel a and the cluster from the computational domain and imposing a zero normal velocity condition at the left-hand face of voxel a. Voxel a in exhibit B also can be eliminated in a similar manner with no consequences for the flow and permeability.

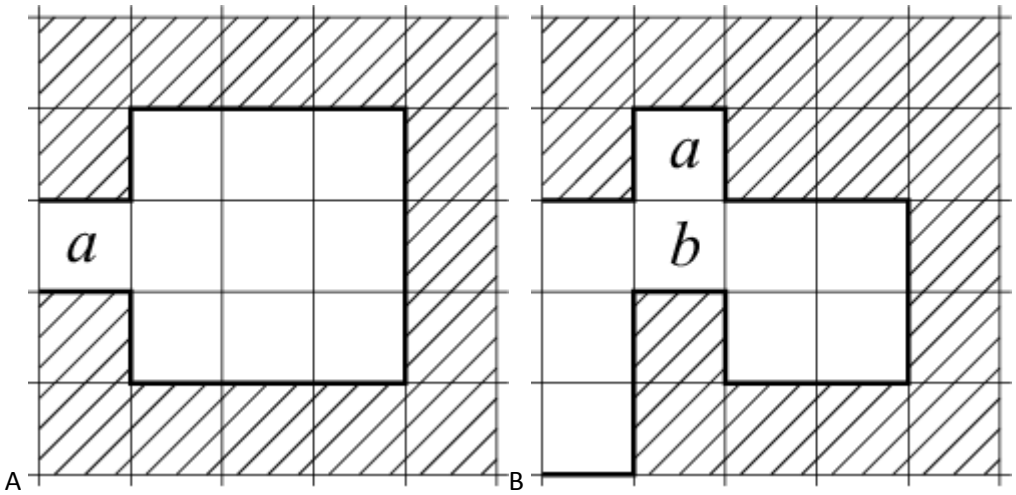

Figure 32. Examples of dead-end voxel configurations.

The argument above suggests an algorithm of dead-end clusters search. First, all voxels with one or two connections to pores through nonadjacent faces should be found by scanning the entire domain. For each voxel with two connections, like in Figure 32 A, one should build two

connected clusters starting on each side. A breadth-first type algorithm similar to one described in [50] can be applied. If either of these clusters is disconnected from the inlet and outlet, it is a dead end and can be removed from the computational domain. It is also a dead end if either both clusters are connected only to the inlet, or both clusters are connected only to the outlet. This connectivity analysis must be applied iteratively, until no more dead-end voxels or clusters are found. For example, voxel b in Figure 32 B has three open boundaries. However, one of these boundaries becomes closed once voxel a is removed. Although neither voxel b nor the entire pore cluster to the right is removed by the first scan, both are defined as dead ends and removed during the second scan.

Relative permeabilities are evaluated assuming capillary equilibrium. In such a case, the distribution of the fluids in the pore space can be estimated using the MIS method. MIS calculations produce a number of capillary-equilibrium fluid distributions. Each distribution is defined by the lists of voxels occupied by the wetting and nonwetting fluid phases. At each saturation, all voxels occupied by one fluid can be considered as a stand-alone pore space. Thus, the permeability of this system of voxels scaled by the absolute permeability of the entire pore space is an approximation to the relative permeability factor.

The following procedure is proposed to evaluate the relative permeability curves numerically.

1. Estimate the absolute permeability of the pore space;
2. For a number of capillary pressures, calculate fluid distribution using MIS algorithm and evaluate the respective saturations;
3. For each fluid distribution, evaluate the permeability to each fluid;
4. Express the relative permeability as a function of saturation.

Simulations can estimate the relative permeability curves for various fluid displacement scenarios. For example, fluid distribution based on ordinary percolation algorithms does not account for the flow path of each phase and is more suitable for estimating relative permeability curves for liquid dropout or gas exsolution. The invasion-percolation algorithms create nonwetting fluid distributions always connected to the sample boundaries, and is suitable for simulating drainage.

Results and Discussions

In MIS calculations, inaccuracy in determination of the pore walls does not affect the radius of an inscribed sphere as much as a single solid voxel incorrectly positioned in the middle of a pore. Therefore, the image cleanup operation described above has a big impact on the capillary pressure evaluation. Figure 33 shows drainage capillary pressure curves computed from a segmented image before and after cluster-search cleanup. The points on the plots are computed from different images from the same sample. The cubic domains are 500 voxels in each direction. The solid curve in Figure 33 is the average value. Although at low capillary

pressures the curves resemble each other very much, they become significantly different as the capillary pressure increases. The reason is that a large portion of the pore volume is disconnected in the raw binary image, and is never accessed by the invading nonwetting fluid. Figure 34 shows simulated gas distribution at two different saturations. In the left-hand picture, the gas phase is connected. In the right-hand picture, connectivity analysis by cluster-search algorithms [49] showed that the gas phase is disconnected. The disconnected bubbles cannot be mobilized because the wetting fluid in the narrow channels connecting larger pores blocks it from moving. Gas bubbles, in turn, block the wetting liquid flow, which results in the Permeability Jail effect.

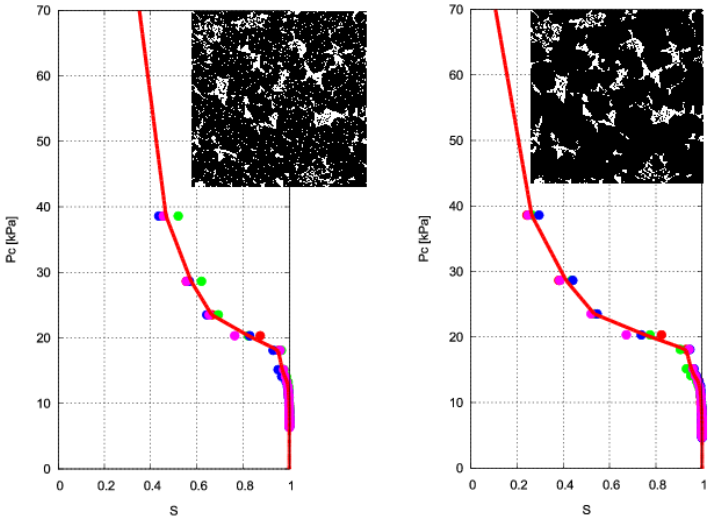

Figure 33. The impact of cluster-search cleanup on the capillary pressure curve evaluation.

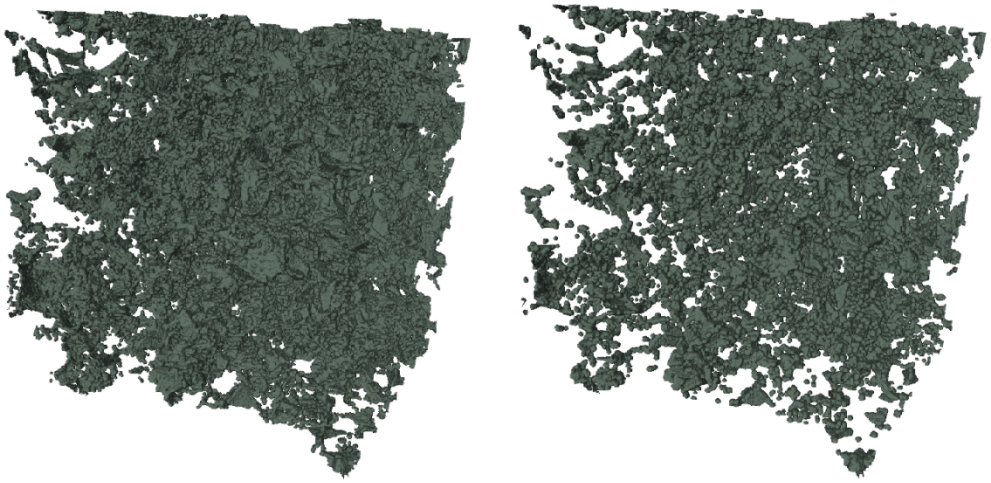

Figure 34. Computed gas distribution in the pores before (left) and after (right) being disconnected.

In Figure 33, the gas invasion was simulated in all directions. Figure 35 shows capillary pressure curves computed by simulations of directional invasion in three coordinate directions: x, y, and z. The computations were performed on an image cleaned by cluster search. The closeness of the computed data points to the mean curve indicates the representativeness of the image.

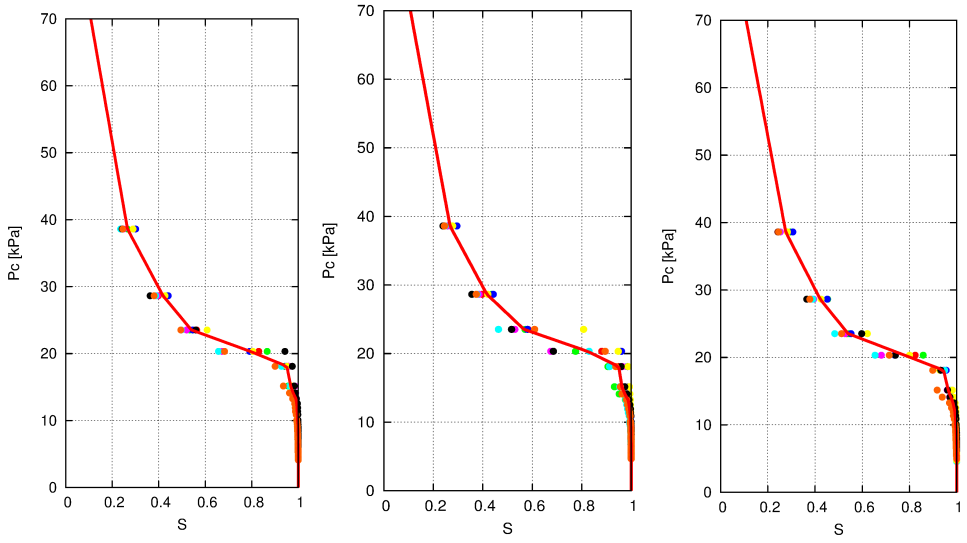

Figure 35. Capillary pressure curves evaluated from invasion percolation in three coordinate directions: x (left), y (middle), and z (right).

Simulations highlight a distinctive feature of tight sand samples: a relatively small volume of the wetting fluid can be sufficient to disconnect the nonwetting phase. The computed saturation threshold estimates this disconnection to occur are near 30 %. Apparently in the studied tight sand samples, the clusters of relatively large pores are connected by narrow channels. Such

structure facilitates gas blockage by the wetting liquid when the latter creates capillary barriers in these narrow connections.

Figure 36 shows plots of numerical results for CT images of sandstone show a number of experimental points obtained in core flood laboratory experiments. The images of the rock pore space used in the computations were not acquired from the same samples, thus the comparison can be only qualitative. One can see that the computed relative permeability curves, which are solid curves with various markers on the plots, are in the same range as the experimental points. The variability of the computed relative permeabilities is similar to that of the data. The partitioning of the 3D image into layers was done differently for different computed curves. The outlier pair of relative permeability curves marked with squares was obtained from a smaller fragment of the image than the other curves.

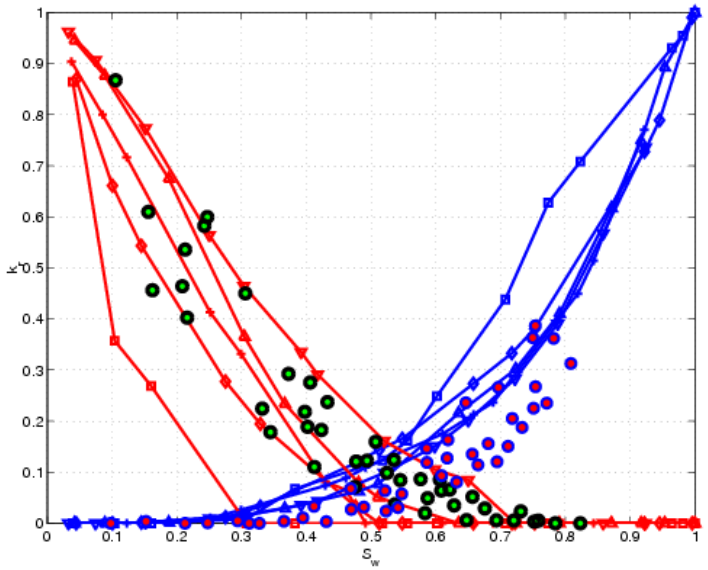

Figure 36. Computed relative permeability curves and laboratory data (circles). The laboratory data are courtesy of Statoil.

Figure 37 shows plots of estimated relative permeability values, shown as diamonds for imbibition and crosses for drainage. The average curves are shown as solid and dot-dashed line respectively. Laboratory gas relative permeability data are displayed as triangles for imbibition and as squares for drainage. The data are courtesy of Chevron. Although the relative positions of computed and measured relative permeability curves are similar, quantitatively they are not the same. This discrepancy can be partially explained by the presence of wetting liquid in small pores and crevices. Imaging these microporosity features would require a higher resolution. The microporosity liquid saturation can be affected only at a very high capillary pressure. Due to the limited image resolution, such capillary pressures are not reached in simulations. Rescaling of the relative permeability curves by introduction of a microporosity saturation would improve the quality of data matching. However, since this microporosity saturation is an unknown quantity, it would appear as a fitting factor. Thus, the results are plotted without any corrections.

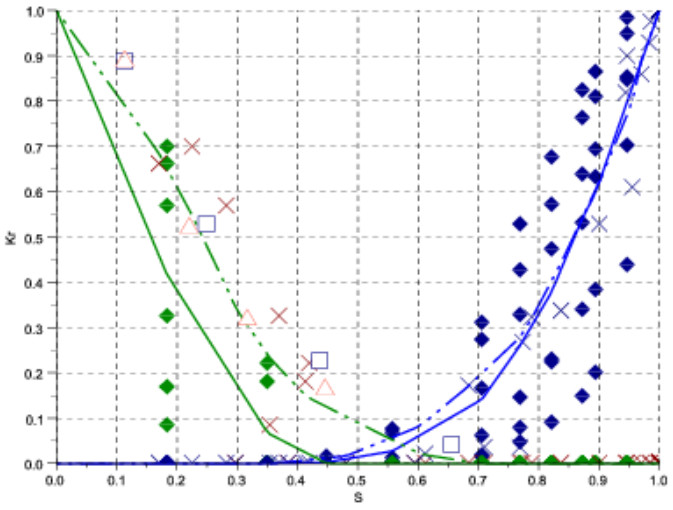

Figure 37. Computed relative permeability data (diamonds for imbibition and crosses for drainage) and laboratory measurements (triangles for imbibition and squares for drainage) of gas relative permeability for different water saturations. The solid lines display mean computed imbibition relative permeability curves, and the dashed curves show mean computed drainage relative permeability curves. The laboratory data are courtesy of Chevron.

Figure 38 shows the results of drainage and imbibition relative permeability evaluation on a micro-CT data set from a different sample. The resulting curves are qualitatively similar to those in Figure 37. Notice however, that the intersection of the imbibition relative permeability curves is a single point, whereas in Figure 37 these curves intersect over an interval of saturations.

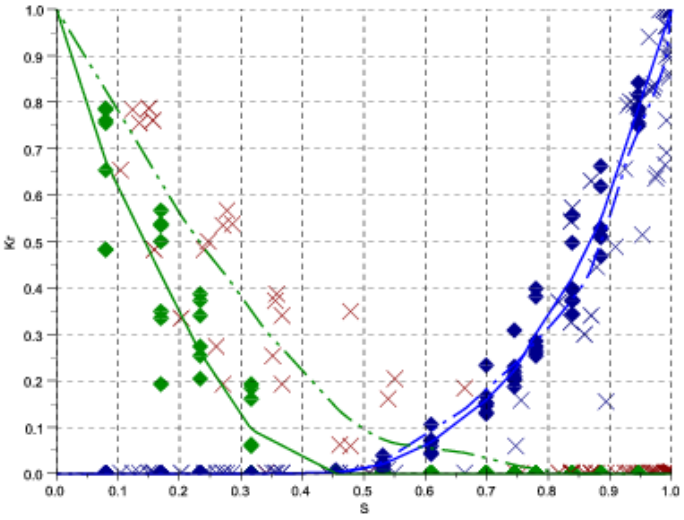

Figure 38. Evaluation of relative permeability curves using MIS analysis and flow simulations. Diamonds denote imbibition relative permeabilities, crosses correspond to drainage. The solid lines show mean imbibition, and the dashed lines show mean drainage curves.

A number of common features are confirmed in all simulations. The nonwetting fluid relative permeability data points are more scattered than those for the wetting fluid. This observation was also valid for conventional rocks [51]. Apparently, the reason for scattering is the possibility of disconnecting the nonwetting phase. In these samples, the relative permeability to gas vanishes as brine saturation approaches 30–40 %.

The absolute permeability of the rock is small, and liquid viscosity exceeds that of gas by orders of magnitude. Therefore, in the range of saturations where the gas relative permeability is zero and liquid relative permeability is close to zero, the gas is immobile. Although theoretically the wetting liquid is always connected, the liquid mobility is extremely low and it is practically trapped. This observation explains the pore-scale nature of "Permeability Jail" [47,14]. The nature of gas trapping is capillarity: the geometry of the pore space creates a distributed liquid capillary barrier breaking gas connectivity. The wetting liquid, even though connected through the corners and crevices in the pores, is trapped dynamically.

In drainage, the invading gas always remains connected. Thus, for a given liquid saturation, the gas permeability in drainage is higher than in imbibition. Note that the drainage relative permeability curves in Figures 37 and 38 intersect above zero, which means that both fluid are mobile. The permeability to liquid for medium saturations in drainage is higher than in the imbibition since connected gas phase is distributed more compactly than dispersed bubbles. Apparently, some liquid flow paths can be totally gas-free. This configuration is different for high liquid saturations, where all gas saturation is concentrated near the inlet pores. Such gas distribution is, apparently, the most-efficient for hindering liquid flow.

More results of MIS and flow simulations are presented in Task 8. For a more detailed technical discussion of capillary pressure and relative permeability evaluation see attached document.

Task 8: Computer models of tight gas rocks

Objectives

The resolution of the micro CT images of samples of tight rock may be insufficient for flow simulations. For example, Figure 20 shows a high-contrast micro CT image of tight sand obtained at a state-of-the-art Xradia machine. However, the slit-like pores in Figure 20 are just a few pixels across. Even though the pixel size is half a micron, extraction of binary data suitable for MIS and flow simulations is difficult, if even possible. The objective of this task is to develop approaches to generation of digital data mimicking natural rocks in a computer. In particular, it is interesting to reproduce some pore geometry features and study the consequences of such features for two-phase flow properties of the medium.

Needless to say, generation of pore structures in a computer does not require expensive imaging tools, it is less time consuming, and computer-generated images can be digitized with

an arbitrary resolution. In addition, segmentation of such data is straightforward. Thus, computer-generated data are ready for modeling.

Methods

The method developed here relies on granular mechanics for computing grain centers [29], it employs Voronoi tesselation to define polyhedral grains [2], and space transformation to finally create the desired porous structure. To build Voronoi diagrams and define grains, we customized some procedures included in QuickHull algorithms [4]. We validate the approach by reconstructing conventional sandstone and comparing capillary pressure curves evaluated with MIS method for computer-generated and microtomography data. The computer rock model is extended to generate structure mimicking slit-like pores, for which we estimate capillary pressure and relative permeability curves. We also propose methods to simulate clay-filling microporosity.

Results and Discussions

Figure 39 shows an example of granular structure generated by the algorithm described above, and micro CT data of Bentheim sandstone. The dark areas in the microtomography data correspond to the exposures of pores. In the computer-generated medium, the pores are transparent. The computed sample is visually similar to Bentheim. The porosity of computer-generated sample is 22 %, whereas the sandstone sample porosity is estimated at 20 %. Interestingly, even though the resolution of the “virtual rock” image is almost twice coarser than that of the sandstone, the dimensionless capillary pressure curves are close to each other (see Figure 40). The curves were computed using the method of Maximal Inscribed Spheres [54,49,58] for two contact angles: 0° and 45°.

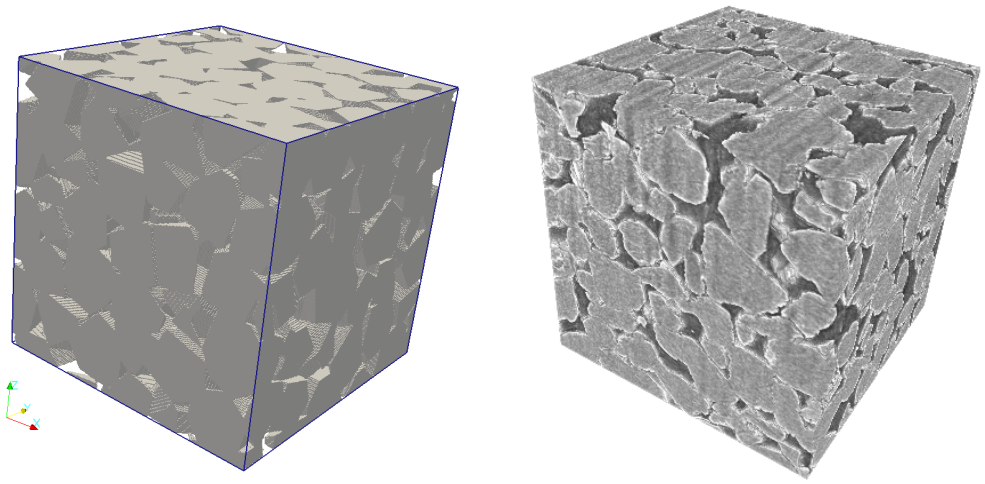

Figure 39. Digitized computer-generated porous structure, on the left, and gray-scale micro CT data for a sample of Bentheim sandstone with voxel size 4.42 μm, on the right.

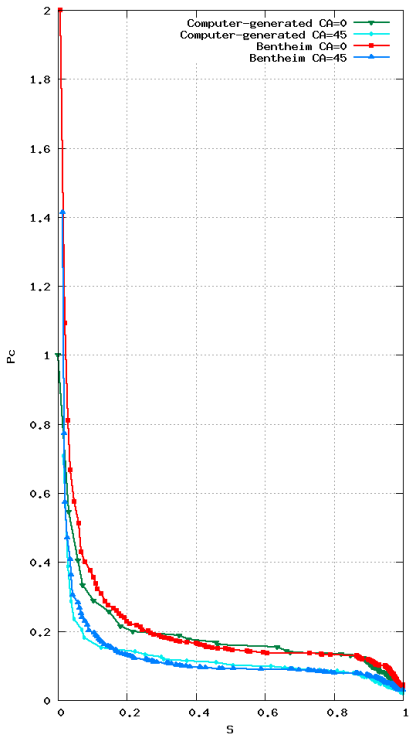

Figure 40. Dimensionless capillary pressure evaluated from images of computer-generated and natural rock samples for two different contact angles (CA).

The computer-generated structure shown in Figure 41 was obtained using the procedure described above with small random rotations and only slight shrinking of the grains. The same medium can model a fractured rock with low-permeability blocks and a connected network of fractures.

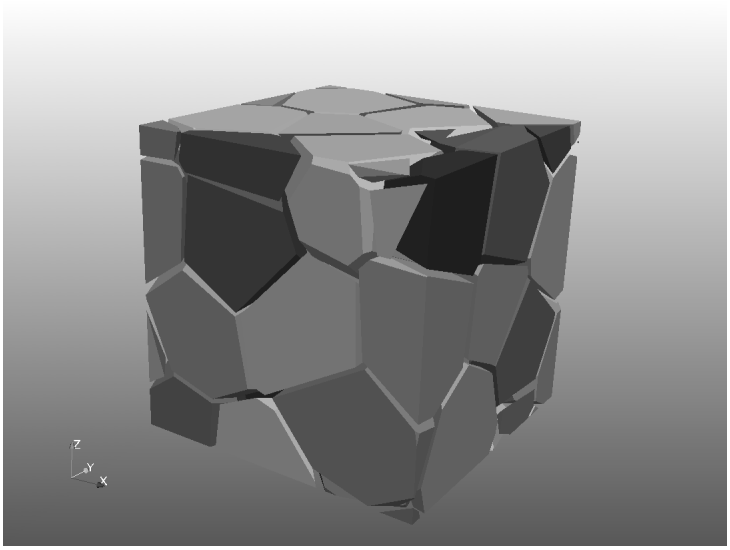

Figure 41. Computer-generated structure with slit-like narrow pores

The images were digitized at two resolutions producing two data sets: $250\times250\times250$ and $500\times500\times500$ voxels. Figure 42 shows drainage capillary pressure curves evaluated for two contact angles for both resolutions by the method of Maximal Inscribed Spheres. The curves are dimensionless. They data can be easily transformed into physically meaningful units by applying scaling factor accounting for the interfacial tension and voxel size. For instance, for a surface tension coefficient of 0.07 N/m and voxel size 0.1 μ m, a multiplication of the dimensionless pressures by 700 will produce capillary pressure in kPa.

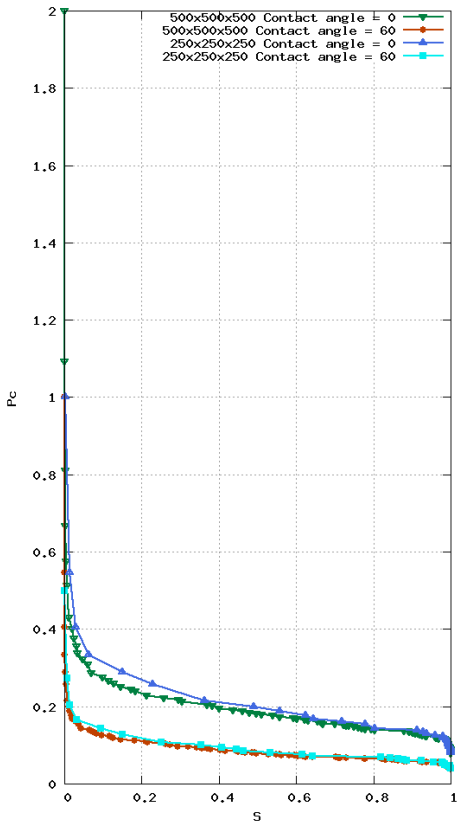

Figure 42. Dimensionless capillary pressure curves computed for different resolutions and two contact angles

Figure 43 show relative permeability curves evaluated for the medium shown in Figure 41. For mixed-wet environment, simulations produce relative permeability curve resembling straight lines. The intersection of the curves for mixed-wet environment is around a common relative permeability value of 0.1, which is almost double the respective value for the wet environment. A distinctive feature of the plots in Figure 43 is that the drainage and imbibition curves almost coincide. The above-zero intersection of the plots in Figure 43 makes them different from the computed relative permeability curves reported in [53]. The latter means that the permeability jail phenomenon [47,14] is pertinent to matrix porosity and is less likely to occur in fractures.

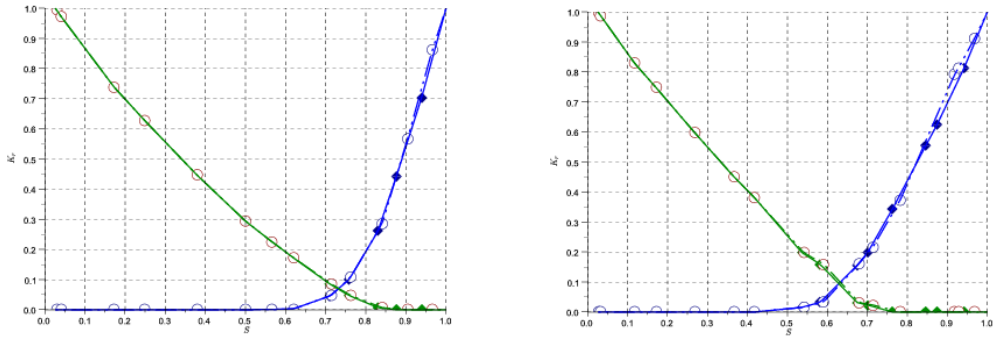

(a) (b)

Figure 43. Relative permeability curves evaluated for media with slit-like pores evaluated for zero, (a), and 60°, (b), contact angles.

The pores in tight-sand samples are partially filled with clay, which creates microporosity [52,53]. The SEM images in Figure 18 show various types of clay at grain surfaces. Microporosity associated with these clay structures affects flow properties of the rock and has to be incorporated into the idealized model of the rock described above. To model microporosity, we generate clusters of grains of special form that mimic clay structures. Figure 44 shows two examples of computer-generated structures mimicking clay fillings shown in Figure 18. The structure in exhibit (a) was generated by translation and rotation of two hexagonal plates. To generate structure (b), the plates were rotated in space by random angles.

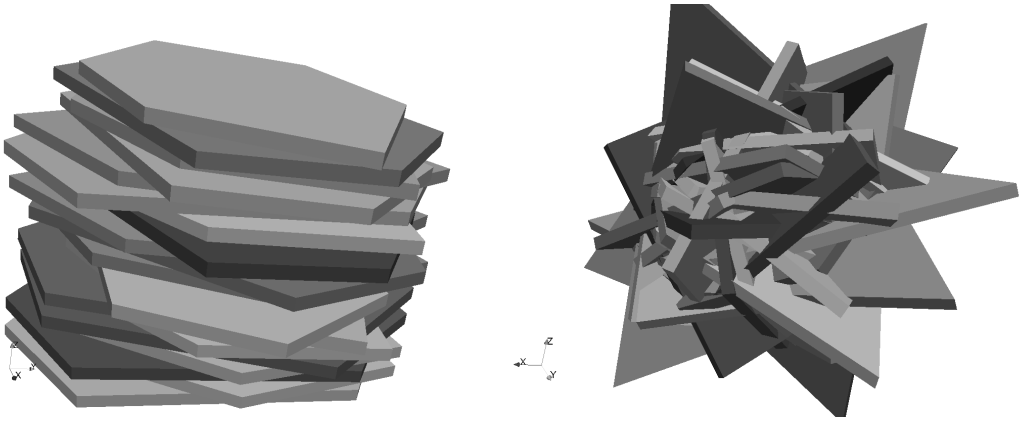

(a) (b)

Figure 44. Computer-generated structures to mimic pore fillings by clay, *cf* Figure 18.

Conclusions

Different imaging techniques cover different scales and resolution and produce 2D or 3D data. With a low-resolution medical scanner one can detect fractures and analyze other irregularities in the reservoir cores. Low-resolution tomography was also used to define the preferences for selecting subsamples for micron-scale x-ray computed microtomography (micro-CT) at the Advanced Light Source facility tomography beamline 8.3.2 to avoid extremes and irregularities. High-resolution imaging reveals the complex pore-space geometry of tight rock but, at the same time, imposes strict constraints on the sample size. An optical microscope and scanning electron microscope were used for verification of the micro-CT reconstructed images and examination of the pore filling structures, which are poorly defined in the micro-CT data. Nanometer-scale resolution of electron microscopy can provide a glimpse into the intergranular microporosity in tight sands and pore structure of shale. The FIB/SEM technique reveals spatial distribution of a rich variety of minerals and kerogen inclusions in 3D.

Custom numerical codes and publicly available libraries were used to analyze the microtomography digital data. The method of Maximal Inscribed Spheres computes capillary-equilibrium fluid distribution for two-phase flow. Simulation of invasion percolation generates drainage capillary pressure curves, whereas ordinary percolation produces imbibition capillary pressure curves. Although the approach used in this study focuses on a volume measured in hundreds of microns to millimeters, the obtained results are self-consistent, and consistent with other measurements. We interpret this consistency as the validation of the method and the representativeness of the samples.

Capillary pressure curves were computed for samples whose 3D reconstructions show sufficient porosity. In some samples, however, the inter-granular void space consists of slit-like pores just few microns across. Such features present difficulty for imaging and can complicate fluid-flow modeling and simulations. For evaluation of capillary-equilibrium fluid distribution and flow properties of such rock we have developed computer-generated structures mimicking the real-rock pore space geometry.

The finite-difference flow simulator developed within the present study can evaluate relative permeability curves from the fluid distributions predicted by the method of Maximal Inscribed Spheres. Although the computed curves are in agreement with laboratory data, evaluation of permeability by flow simulations is the most computationally intense part of computations. The size of the computational domain is limited by the available computing power. Decoupling relative permeability evaluations for different saturations makes it possible to run simulations on multiple cores or computers independently of each other. All computations in this study were performed using a desktop computer, without resorting to massive-parallel machines.

From our work, we have observed the following:

The drainage capillary pressure curves computed for tight-sand samples show capillary barriers exceeding those evaluated for conventional sandstones. It is an indication of narrow inter-pore

connections hindering the invasion of the nonwetting fluid (gas). Simulations show that the saturation connectivity threshold for tight sands is unusually low. If simulations for conventional sandstones show that the nonwetting fluid may stay connected at water saturation near 70%, simulations on images of tights and samples show that 30% wetting fluid saturation can make the gas phase disconnected. This observation suggests the capillary nature of gas trapping by water or gas condensate. Computed relative permeability to gas vanishes at saturations near 30%. The water relative permeability curve intersects the gas permeability curve near zero. This means that gas and water flows are mutually exclusive. Gas may be disconnected but still present in the form of bubbles, however. These bubbles occupy the central parts of the pores leaving narrow passages for the wetting fluid flow. Since water or gas condensate viscosity is much higher than that of gas, the mobility of the wetting fluid is very low except at almost full saturation where the water relative permeability approaches one. This observation explains the pore-scale mechanism of the so-called Permeability Jail reported in the literature: there exists a range of saturations where no fluid flow is possible. The nature of gas flow blocking by water or condensate is capillary, whereas the wetting fluid flow blocking is both dynamic (low permeability in the pore corners) and capillary (dispersed gas bubbles).

A simple pore-scale model of retrograde gas condensation suggests that the rate of dropout scales with the dot product of the pressure gradient and fluid velocity. This model naturally upscales to Darcy-flow scale, where the retrograde condensation rates are proportional to the pressure gradient squared. Simulation of gas flow in a capillary tube of variable cross-section diameter shows that the condensate dropout rate is higher in the narrow parts than that in a wider tube part with the proportionality coefficient equal to the inverse ratio of the radii raised to the fourth power. Thus, retrograde condensation will promote clogging the narrow pore throats, which will lead to further disconnection and pore-scale compartmentalization of the gas phase. Because of the Permeability Jail, a small amount of condensate may completely block gas flow.

An optimal-control gas flow model employs the pore-scale modeling results to account for the liquid skin buildup at fracture-matrix interface. The optimization criterion evaluates total gas recovery over a given period of time. Forward calculations show strong dependence of the criterion on fracture pressure. Calculations yield that the optimal fracture pressure regime seeks to stabilize the flow rate over the entire period of time, as opposed to uncontrolled high initial rate followed by fast production decline. The model is highly idealized and needs further development and verification to be linked to a reservoir simulator for realistic output. However, our preliminary calculations suggest that production pressure and rate control has potential for reducing the adverse impact of retrograde condensation and for significant ultimate gas recovery increment.

Imaging studies of reservoir shale samples reveal rock heterogeneity in many scales. Low-resolution CT data show layered structure of the rock. Nanometer-scale imaging with FIB/SEM technology shows that even a volume of tens of microns across includes arch variety of minerals, grain shapes and sizes, inter granular organic-matter pore fillings. Samples from

different basins and formations are different from each other. Some images, like those of Barnett shale, show pores both in organic and mineral phases. At the same time, images of New Albany shale show almost no porosity even at a resolution of 14 nanometers per pixel. The observed organic contents in images of gas shale samples is greater than that in images of quarry shale. At the same time, the organic-matter saturation of oil shale is higher than that for gas shale.

The representativeness of a typical volume of investigation for nanometer-scale imaging is uncertain. Nevertheless, the findings of this study are in a reasonable agreement with other nanometer-scale gas shale imaging results reported in the literature. Extension of the imaging database would increase the confidence in the validity of results.

In spite of the rich variety of the gas-shale structures revealed by the imaging study, all studied samples show very low permeability of the rock matrix. This observation lead us to a model of gas flow to a fractured well. In this model, the permeability of the pristine reservoir is negligible, and gas flow occurs only in the limited stimulated reservoir volume adjacent to the fracture. The inferred initial- and boundary-value problem is nonlinear with no known analytical solution. A technique based on the method of integral relations produces an approximate solution in an exact form, which correlates the well production decline rates to the reservoir properties. In fact, numerical simulations verify the approximate solution. Moreover, the obtained approximate solution reproduces the production data from a number of gas well. One of the model predictions is that the production rate declines in a bimodal manner. In early times, when the production yet is not affected by the boundaries of the stimulated zone, the recovery rate declines as the square root of time. At later times, the decline rate is exponential. The data from a number of gas shale wells confirm this model prediction.

The study described in this report is a basic step towards understanding of tight gas recovery mechanisms. Physical processes occur at different scales, from nanometer-size pores to reservoirs and basins. Understanding of these processes and interpreting them across the spatial and temporal scales will require additional more laboratory, theoretical, and modeling research.

Acknowledgements

This work has been performed at Lawrence Berkeley National Laboratory (LBNL) of the U.S. Department of Energy (DOE) under Contract No. DE-AC02-05CH11231. Synchrotron microtomography was performed at the Advanced Light Source facility (ALS), Beamline 8.3.2, which is supported by the Office of Science, Office of Basic Energy Sciences, of the U.S. DOE (contract DE-AC02-05CH11231). FIB/SEM and EDX imaging was performed at the Molecular Foundry and The National Center for Electron Microscopy (NCEM), LBNL, which are supported by the Office of Science, Office of Basic Energy Sciences, of the U.S. Department of Energy under Contract No. DE-AC02-05CH11231. Xradia, Inc. and Gatan, Inc. are acknowledged with gratitude for sharing their innovative imaging technologies and acquiring high-resolution data at their

facilities. The reservoir gas tight sand samples used in this study were shared by BP and Chevron. Shale samples were shared by Chevron, Whiting Petroleum, Schlumberger, Gas Technology Institute (GTI), and Texas Bureau of Economic Geology (BEG).

Funding for this project was provided by Research Partnership to Secure Energy for America (RPSEA) through the "Ultra-Deep-water and Unconventional Natural Gas and Other Petroleum Resources" program authorized by the U.S. Energy Policy Act of 2005. RPSEA (www.rpsea.org) is a nonprofit corporation whose mission is to provide a stewardship role in ensuring the focused research, development and deployment of safe and environmentally responsible technology that can effectively deliver hydrocarbons from domestic resources to the citizens of the United States. RPSEA, operating as a consortium of premier U.S. energy research universities, industry, and independent research organizations, manages the program under a contract with the U.S. DOE's National Energy Technology Laboratory.

The authors acknowledge with gratitude discussions with Joanne Friedrich of BP, Rafael Salazar-Tio, Jairam Kamath, Josephine Schembre, Padmakar Ayyalasomayajula, and Luca Duranti of Chevron, Marc Thiercelin and Supratik Banerji of Sclumberger, Michael Willson of Whiting Petroleum, Iraj Salehi of GTI and Julia Gale of BEG, Mark Shannon and Hesham El-Sobky of ConocoPhillips. Andrew Mei of LBNL Engineering prepared the samples for imaging at the Molecular Foundry and ALS. Alastair McDowell of the ALS helped with microtomography imaging. Stefano Cabrini of the Molecular Foundry helped with experimental setup and technical advice. The authors are thankful to Velimir Radmilovic of NCEM for helping with elemental mapping. Velimir Radmilovic and Liviu Tomutsa of LBNL Earth Sciences Division are the original developers of the FIB/SEM imaging techniques employed in this work. Discussions with professor M. Panfilov of University of Nancy, France, and professor G. Barenblatt of University of California, Berkeley, helped to develop the condensate dropout model.

Literature

[1] Gus Alvarado, J. L. Le Blanc, and F. Farshad, *A new and improved material balance equation for retrograde gas condensate reservoirs – Part I. SPE paper 24355*, SPE Rocky Mountain Regional Meeting, 18-21 May 1992, Casper, Wyoming, 1992.

[2] Franz Aurenhammer, *Voronoi diagrams — a survey of a fundamental geometric data structure*, ACM Comput. Surv. **23** (1991), no. 3, 345–405.

[3] F. M. Auzerais, J. Dunsmuir, B. B. Ferreol, N. Martys, J. Olson, T. S. Ramakrishnan, D. H. Rothman, and L. M. Schwartz, *Transport in sandstone: A study based on three dimensional microtomography*, Geophysycal Research Letters **23** (1996), 705–708.

[4] C. B. Barber, D. P. Dobkin, and H. T. Huhdanpaa, *The Quickhull algorithm for convex hulls*, ACM Trans. on Mathematical Software **22** (1996), 469–483.

[5] Robert W. Barber and David R. Emerson, *Challenges in modeling gas-phase flow in microchannels: From slip to transition*, Heat Transfer Engineering **27** (2006), no. 4, 3–12.

[6] G. I. Barenblatt, *On some approximate methods in the theory of one-dimensional unsteady filtration in the elastic drive regime*, Izvestiya (Bulletin), USSR Academy of Sciences, Division of Technical Sciences (in Russian) (1954), no. 9, 35–49.

[7] G. I. Barenblatt, *The mathematical model of the flow of gas-condensate mixtures in fissurized porous rocks with an application to the development of tight sand gas deposits*, Proceedings of the Second International Symposium on Dynamics of Fluids in Fractures Rocks (Boris Faybishenko and Paul A. Witherspoon, eds.), Lawrence Berkeley National Laboratory, 2004, p. 268.

[8] G. I. Barenblatt, K. S. Basniev, and I. N. Kochina, *On basic concepts of the theory of flow of gas-condensate mixtures in fissurized-porous rocks*, Izvestiya (Bulletin), Azerbaidjanian Academy of Sciences, Earth Sciences (in Russian) (1988), no. 5, 3–17.

[9] G. I. Barenblatt, V. M. Entov, and V. M. Ryzhik, *Theory of fluid flows through natural rocks*, Kluwer Academic Publishers, Dordrecht, 1990.

[10] Stephen Brunauer, Lola S. Deming, W. Edwards Deming, and Edward Teller, *On a theory of the van der Waals adsorption of gases*, Journal of the American Chemical Society **62** (1940), no. 7, 1723–1732.

[11] Stephen Brunauer, P. H. Emmett, and Edward Teller, *Adsorption of gases in multimolecular layers*, Journal of the American Chemical Society **60** (1938), no. 2, 309–319.

[12] A. J. Chorin, *A numerical method for solving incompressible viscous flow problems*, Journal of Computational Physics **2** (1967), 12–26.

[13] A. J. Chorin, *Numerical solution of the Navier–Stokes equations*, Math. Comp. **22** (1968), 745–762.

[14] Robert M. Cluff and Alan P. Byrnes, *Relative permeability in tight gas sandstone reservoirs – the "Permeability Jail" model*, SPWLA 51st Annual Logging Symposium, June 19-23, 2010.

[15] M. E. Coles, R. D. Hazlett, E. L. Muegge, K. W. Jones, B. Andrews, Dowd, P. Siddons, and A. Peskin, *Developments in synchrotron X-ray microtomography with applications to flow in porous media*, SPE Reservoir Evaluation and Engineering **1** (1998), no. 4, 288–296.

[16] M. E. Coles, R. D. Hazlett, P. Spanne, E. L. Muegge, and M. J. Furr, *Characterization of reservoir core using computed microtomography*, SPE Journal **1** (1996), no. 3, 295–302.

[17] M. E. Coles, R. D. Hazlett, P. Spanne, W. E. Soll, E. L. Muegge, and K. W. Jones, *Pore level imaging of fluid transport using synchrotron X-ray microtomography*, Journal of Petroleum Science and Engineering **19** (1998), 55–63.

[18] R. G. Deissler, *An analysis of second-order slip flow and temperature-jump boundary conditions for rarefied gases*, Journal of Heat and Mass Transfer **7** (1964), 681–694.

[19] Ana Diaz, Pavel Trtik, Manuel Guizar-Sicairos, Andreas Menzel, Pierre Thibault, and Oliver Bunk, *Quantitative x-ray phase nanotomography*, Phys. Rev. B **85** (2012), no. 2, 020104.

[20] M. Dierick, B. Masschaele, and L. Van Hoorebeke, *Octopus, a fast and user-friendly tomographic reconstruction package developed in LabView®*, Measurement Science and Technology **15** (2004), 1366–1370.

[21] Jack Dongarra, Andrew Lumsdaine, Xinhiu Niu, Pozo Roldan, and Karin Remington, *A sparse matrix library in C++ for high performance architectures*, Proceedings of the Second Object Oriented Numerics Conference, 1994.

[22] M. D. Donohue and G. L. Aranovich, *Adsorption hysteresis in porous solids*, Journal of Colloid and Interface Science **205** (1998), no. 1, 121 – 130.

[23] M. M. Dubinin, *The potential theory of adsorption of gases and vapors for adsorbents with energetically nonuniform surfaces.*, Chemical Reviews **60** (1960), no. 2, 235–241.

[24] Julia F. W. Gale, Robert M. Reed, and Jon Holder, *Natural fractures in the Barnett Shale and their importance for hydraulic fracture treatments*, AAPG Bulletin **91** (2007), no. 4, 603–622.

[25] Philip E. Gill, Walter Murray, and Margaret H. Wright, *Practical optimization*, Academic Press, 1981.

[26] T. R. Goodman, *The heat-balance integral and its application to problems involving a change of phase*, Transaction of ASME **80** (1958), 335–342.

[27] Gabor T. Herman, *Image reconstruction from projections: The fundamentals of computerized tomography*, Academic Press, New York, 1980.

[28] J. O. Hirschfelder, C. F. Curtiss, and R. B. Bird, *Molecular theory of gases and liquids*, John Wiley and Sons,, New York, 1954.

[29] R. Holtzman, D. B. Silin, and T. W. Patzek, *Mechanical properties of granular materials: A variational approach to grain-scale simulations*, International Journal for Numerical and Analytical Methods in Geomechanics **33** (2009), no. 3, 391–404.

[30] J. H. Kinney and M. C. Nichols, *X-ray tomographic microscopy (xtm) using synchrotron radiation*, Annual Review of Materials Science **22** (1992), no. 1, 121–152.

[31] L. J. Klinkenberg, *The permeability of porous media to liquids and gases*, Drilling and Production Practice, American Petroleum Institute, 1941.

[32] G. Kowalski, *Suppression of ring artifacts in fan-beam scanners*, Journal of Computer Assisted Tomography **1** (1977), no. 2, 266.

[33] L. D. Landau and E. M. Lifschitz, *Fluid mechanics*, Series in advanced physics, vol. 6, Addison-Wesley, Reading, MA, 1959.

[34] N.Kh. Magerramov and A.Kh. Mirzadzhanzade, *Filtration of gas-condensate mixtures in a porous medium*, Journal of Applied Mathematics and Mechanics **24** (1960), no. 6, 1656 – 1664.

[35] J. C. Maxwell, *On stresses in rarefied gases arising from inequalities of temperature*, Philos. Trans. Royal Soc. London **170** (1879), 231–256.

[36] M. Evans Munroe, *Modern multidimensional calculus*, Addison-Wesley, 1963.

[37] M. Muskat, *Physical principles of oil production*, McGraw-Hill, New York, NY, 1949.

[38] P. E. Øren, S. Bakke, and H. G. Rueslåtten, Digital core laboratory: Rock and flow properties derived from computer generated rocks, International Symposium of the Society of Core Analysts (Trondheim, Norway), Society of Core Analysits, 12-16 September 2006.

[39] I. Panfilova and M. Panfilov, *Near-critical gas liquid flow in porous media: Monovariant model, analytical solutions and convective mass exchange effects*, Transport in Porous Media **56** (2004), 61–85, 10.1023/B:TIPM.0000018391.55013.22.

[40] A. M. Pirverdian, *About a method of approximate solution of elastic-drive filtration problems*, Inzhenernyj Sbornik (in Russian) **14** (1953), 189–191.

[41] P. Ya. Polubarinova-Kochina, *About unsteady coal-bed gas filtration*, Applied Mathematics and Mechanics (in Russian) **17** (1953), no. 6, 735–738.

[42] L. S. Pontryagin, V. G. Boltyanskii, R. V. Gamkrelidze, and E. F. Mischenko, *The mathematical theory of optimal processes*, Interscience Publishers, 1962.

[43] S. Rassenfoss, *Digital rocks out to become a core technology*, Journal of Petroleum Technology (2011), 36–41.

[44] Françoise Rouquerol, Jean Rouquerol, and Kenneth Sing, *Adsorption by powders and porous solids. Principles, methodology and applications*, Elsevier, 1999.

[45] Subrata Roy, Reni Raju, Helen F. Chuang, Brett A. Cruden, and M. Meyyappan, *Modeling gas flow through microchannels and nanopores*, Journal of Applied Physics **93** (2003), no. 8, 4870–4879.

[46] J. Schembre-McCabe, R. Salazar-Tio, G. Ball, and J. Kamath, *A framework to validate digital rock technology. SCA2011-28*, International Symposium of the Society of Core Analysts held in Austin, Texas, USA 18-21 September, 2011 , 2011.

[47] Keith W. Shanley, Robert M. Cluff, and John W. Robinson, *Factors controlling prolific gas production from low-permeability sandstone reservoirs: Implications for resource assessment, prospect development, and risk analysis*, AAPG Bulletin **88** (2004), no. 8, 1083–1121.

[48] Polad M Shikhaliev, *Beam hardening artefacts in computed tomography with photon counting, charge integrating and energy weighting detectors: a simulation study*, 2005, pp. 5813–.

[49] D. Silin and T. Patzek, *Pore space morphology analysis using maximal inscribed spheres*, Physica A. Statistical Mechanics and its Applications **371** (2006), 336–360.

[50] D. B. Silin and T. W. Patzek, *An object-oriented cluster search algorithm*, Tech. Report LBNL-51599, Lawrence Berkeley National Laboratory, 2003.

[51] D. B. Silin and T. W. Patzek, *Predicting relative-permeability curves directly from rock images. SPE 124974*, 2009 SPE Annual Technical Conference and Exhibition (New Orleans, Louisiana, U.S.A.), SPE, 2009.

[52] Dmitriy Silin, Timothy J. Kneafsey, Jonathan B. Ajo-Franklin, and Peter Nico, *Pore-scale mechanisms of gas flow in tight sand reservoirs*, Tech. Report LBNL-4103E, Lawrence Berkeley National Laboratory, November 2010.

[53] Dmitriy Silin, Timothy J. Kneafsey, Jonathan B. Ajo-Franklin, and Peter Nico, *A multimodal 3D imaging study of natural gas flow in tight sands. SPE paper 146611*, SPE Annual Technical Conference and Exhibition, 30 October-2 November 2011, Denver, Colorado, USA, 2011.

[54] Dmitriy Silin, Liviu Tomutsa, Sally Benson, and Tad Patzek, *Microtomography and pore-scale modeling of two-phase fluid distribution*, Transport in Porous Media (2010), 1–21, 10.1007/s11242-010-9636-2.

[55] Cecilia Solar, Andrés García Blanco, Andrea Vallone, and Karim Sapag, *Adsorption of methane in porous materials as the basis for the storage of natural gas*, Natural Gas (Primoz Potocnik, ed.), Sciyo, August 2010, pp. 205–244.

[56] P. Spanne, J. F. Thovert, C. J. Jacquin, W. B. Lindquist, K. W. Jones, and P. M. Adler, *Synchrotron Computed Microtomography of Porous Media: Topology and Transports*, Phys. Rev. Lett. **73** (1994), no. 14, 2001–2004.

[57] Liviu Tomutsa and Velimir Radmilovic, *Focused ion beam assisted three-dimensional rock imaging at submicron scale, SCA2003-47*, International Symposium of the Society of Core Analysts (Pau, France), September 2003.

[58] Liviu Tomutsa, Dmitriy Silin, and Velimir Radmilovic, *Analysis of chalk petrophysical properties by means of submicron-scale pore imaging and modeling*, SPE Reservoir Evaluation and Engineering **10** (2007), no. 3, 285–293.

[59] Olga I. Vinogradova, *Drainage of a thin liquid film confined between hydrophobic surfaces*, Langmuir, 1995, 11 (6), pp 2213–2220 **11** (1995), no. 6, 2213–2220.

[60] Olga I. Vinogradova and G. E. Yakubov, *Surface roughness and hydrodynamic boundary conditions*, Physical Review E **73** (2006), no. 4, 045302.

[61] I. V. Volkov and O. G. Fridlender, *Boundary conditions of gas dynamic slip on a rough surface*, Fluid dynamics **22** (1987), no. 1, 156–159.

Impact to Producers

The interest to the pore-scale study of unconventional oil and gas reserves grew over the duration of this project. Today, several companies provide imaging and data analysis services to producers. Some production companies have developed their own in-house capabilities. The 2011 SPE Digital Rock Forum was well-attended, both by the industry and academia, which reflects the growing interest to this new discipline.

Modeling tools and approaches were also developed within this project. Included are 1) the pressure decline analysis described in Task 4 (above), advances in the Maximal Inscribed Spheres method for computing flow properties including the Klinkenberg coefficient from the digitized images described in Task 7 (above) and new methods for constructing rock models described in Task 8 (above).

Technology Transfer Efforts

The results of conducted research have been shared with the industry and made public through journal and SPE publications, and a number of conference and invited presentations. In October 2009, a workshop "*Numerical Modeling with Large 3D Data Sets*" on micron-scale computed tomography imaging and image processing was held at the Advanced Light Source facility of Lawrence Berkeley National Laboratory. The workshop was attended by engineers and scientists from BP, Chevron, Ingrain, Numerical Rock, Visualization Sciences Group, Xradia, University of Texas at Austin, Stanford University, and, of course, Lawrence Berkeley National Laboratory.

Conference presentations and SPE papers

1. Timothy Kneafsey, Dmitriy Silin, and Stefano Cabrini, "Natural gas production from Shales: Imaging tight media and analysis of flow" presented at the National Center for Electron Microscopy and Molecular Foundry Annual Users Meeting (Oct 4-5, 2012)

2. Dmitriy Silin, Timothy J. Kneafsey, Jonathan B. Ajo-Franklin, and Peter Nico. A Multimodal 3D Imaging Study of Natural Gas Flow in Tight Sands. SPE paper 146611 presented at the SPE

Annual Technical Conference and Exhibition held in Denver, Colorado, USA, 30 October–2 November 2011.

3. Timothy J. Kneafsey, Dmitriy Silin, and Stefano Cabrini. Imaging gas shales: Insights and extension to observed behavior. 2011 The Molecular Foundry (TMF) and the National Center for Electron Microscopy (NCEM) Joint User Meeting, October 5 - 6, 2011.

4. Silin, D. and Kneafsey, T. From pore-scale to well decline curve analysis. 2011 Geological Society of America Annual Meeting, 9-12 October 2011, Minneapolis, Minnesota

5. Silin, D. and Kneafsey, T. Gas shale: from nanometer-scale observations to well modeling. SPE paper 149489 presented at the Canadian Unconventional Resources Conference held in Calgary, Alberta, Canada, 15–17 November 2011.

6. Silin, D. and Kneafsey, T. A study of shale-gas recovery mechanisms. ShaleEnergy Technology Conference. Houston, TX, August 24-25, 2011

7. Silin, D. High Resolution Imaging for Gas Shales. RPSEA Unconventional Gas Conference 2011 Denver, CO April 19 2011.

8. Silin, D., Ajo-Franklin, J. B., Cabrini, S., Kneafsey, T. J., MacDowell, A., Nico, P. S., and Radmilovic, V., Pore-scale studies of gas shale. Abstract MR22C-03 presented at 2010 Fall Meeting, AGU, San Francisco, Calif., 13-17 Dec., 2010.

9. Dmitriy Silin, Timothy J. Kneafsey, Jonathan B. Ajo-Franklin, and Peter Nico. Pore-scale mechanisms of gas flow in tight sand reservoirs. LBNL Report 4103E. November 2010.

10. Dmitriy Silin, Jonathan Ajo-Franklin, Stefano Cabrini, Timothy Kneafsey, Peter Nico, and Velimir Radmilovic FIB/SEM Imaging of Gas Shale Samples. The Molecular Foundry - National Center for Electron Microcopy User's Meeting 2010, Sept. 30 - Oct. 1, 2010.

11. Silin, D., Kneafsey, T., Ajo-Franklin, J., and Nico, P. Three-Dimensional Imaging of Tight Gas Host Rock – Observations and Conceptual Models. Goldschmidt 2010 Conference. Knoxville, TN, June 13-18, 2010.

12. Nico, P. S., Ajo Franklin, J. B., Benson S. M., MacDowell, A., Silin, D. B., Tomutsa, L., and Wu, Y. Synchrotron X-ray Micro-Tomography and Geological CO2 Sequestration.. In Advances in Computed Tomography for Geomaterials, GeoX 2010. Ed. Khalid .A. Alshibi and Allen H. Reed. Wiley, & Sons, Hoboken, NJ, p. 374-380, 2010

13. Silin, D. High Resolution Imaging for Gas Shales. RPSEA Unconventional Gas Project Review Meeting Denver, CO April 06, 2010

14. Silin, D., Ajo Franklin, J. B., Cabrini, S., Kneafsey, T. J., MacDowell, A. Nico, P. S., and Tomutsa, L. Pore-scale studies of unconventional reservoir rocks. Eos Trans. AGU, 90(52), Fall Meet. Suppl., Abstract H23F-1018, 2009

15. Analyzing microtomography images of natural rocks with the method of maximal inscribed spheres. Numerical Modeling with Large 3D Data Sets, ALS Workshop, October 17, 20091

16. Silin, D. and Patzek, T. Predicting Relative-Permeability Curves Directly From Rock Images. SPE paper 124974 presented at the SPE Annual Technical Conference and Exhibition, 4-7 October 2009, New Orleans, Louisiana, 2009. Society of Petroleum Engineers

17. Silin, D. Petrophysical studies of unconventional gas reservoirs using high-resolution rock imaging. RPSEA Unconventional Gas Project Review Meeting Denver, CO, April 15, 2009

Invited presentations

1. Imaging and Modeling Studies of Gas Flow in Tight Reservoirs. Chevron, San Ramon, CA March 29 2012.

2. Imaging and Modeling Studies of Natural Rocks. ConocoPhillips, Houston, TX, March 27 2012.

3. Imaging and modeling studies of shale-gas recovery mechanisms (with T. Kneafsey and J. Ajo-Franklin). 8th Annual Meeting of the Physics and Application of Seismic Emission (PHASE) Consortium. Free University of Berlin, Berlin, Germany, February 24 2012.

4. Imaging and Modeling Tight Gas Rocks. Ingrain Inc. Houston, TX, August 26 2011

5. Imaging and modeling gas shales. Chevron, San Ramon, CA March 22 2011

6. Pore-scale studies of fluid displacement and trapping mechanisms in natural rocks. International Research Institute of Stavanger. Stavanger, Norway, January 24 2011

7. High Resolution Imaging for Gas Shales, an update. Chevron, San Ramon, CA, June 10, 2010.

8. Pore-Scale Modeling of Two-Phase Flow in Natural Rocks. Stanford University, June 10, 2009.

9. Development and Verification of a Pore-Scale Model of Natural Rocks. University of Texas, Austin, April 20, 2009

Journal publications (published, in press, and under review)

1. Silin, D., Tomutsa, L., Benson, S. R., and Patzek, T. W. Microtomography and pore-scale modeling of two-phase fluid distribution. Transport in Porous Media, 2011, 86, No. 2, p. 525-54.

2. Silin, D. and Kneafsey, T. From pore-scale to well decline curve analysis. Journal of Canadian Petroleum Technology, in press

3. Silin, D. An optimal-control model for gas recovery in tight formations. Optimization and engineering, in review

4. Cortis, Andrea, and Silin, D. Numerical evaluation of relative permeability using Johnson-Koplik-Dashen model, submitted

LIST OF ACRONYMS AND ABBREVIATIONS

ALS	Advanced Light Source facility
BIB	Broad Ion Beam
CCD	charge coupled device
CT	Computed tomography
EBSD	Electron Back Scatter Diffraction
EDS	energy-dispersive X-ray spectroscopy
EELS	electron energy loss spectroscopy
FIB	Focused Ion Beam
LBNL	Lawrence Berkeley National Laboratory
MIS	Maximal Inscribed Spheres
SEM	Scanning Electron Microscope
SPE	Society of Petroleum Engineers
WDS	wavelength dispersive spectroscopy

APPENDICES

Appendices are attached as separate files.

Silin, Dmitriy. (2009). A pore-scale model of two-phase flow in water-wet rock. Lawrence Berkeley National Laboratory: Lawrence Berkeley National Laboratory. Retrieved from: http://www.escholarship.org/uc/item/7bn9m7d9